SUBMITTED TO ApJS; astro-ph/0610739
Preprint typeset using LaTeX style emulateapj v. 10/09/06

THE 400 SQUARE DEGREES *ROSAT* PSPC GALAXY CLUSTER SURVEY: CATALOG AND STATISTICAL CALIBRATION

R. A. BURENIN[1], A. VIKHLININ[2,1], A. HORNSTRUP[3], H. EBELING[4], H. QUINTANA[5], A. MESCHERYAKOV[1]

Submitted to the Astrophysical Journal Supplement Series October 25, 2006. astro-ph/0610739

ABSTRACT

We present a catalog of galaxy clusters detected in a new *ROSAT* PSPC survey. The survey is optimized to sample, at high redshifts, the mass range corresponding to $T > 5\,\mathrm{keV}$ clusters at $z = 0$. Technically, our survey is the extension of the 160 square degrees survey (160d, Vikhlinin et al. 1998a; Mullis et al. 2003). We use the same detection algorithm, thus preserving high quality of the resulting sample; the main difference is a significant increase in sky coverage. The new survey covers 397 square degrees and is based on 1610 high Galactic latitude *ROSAT* PSPC pointings, virtually all pointed *ROSAT* data suitable for the detection of distant clusters. The search volume for X-ray luminous clusters within $z < 1$ exceeds that of the entire local Universe ($z < 0.1$). We detected 287 extended X-ray sources with fluxes $f > 1.4 \times 10^{-13}\,\mathrm{erg\,s^{-1}\,cm^{-2}}$ in the 0.5–2 keV energy band, of which 266 (93%) are optically confirmed as galaxy clusters, groups or individual elliptical galaxies. This paper provides a description of the input data, the statistical calibration of the survey via Monte-Carlo simulations, and the catalog of detected clusters. We also compare the basic results to those from previous, smaller area surveys and find good agreement for the $\log N$–$\log S$ distribution and the local X-ray luminosity function. Our sample clearly shows a decrease in the number density for the most luminous clusters at $z > 0.3$. The comparison of our *ROSAT*-derived fluxes with the accurate *Chandra* measurements for a subset of high-redshift clusters demonstrates the validity of the 400 square degree survey's statistical calibration.

Subject headings: catalogs — galaxies: clusters: general — surveys — X-rays: galaxies

1. INTRODUCTION

Observations of galaxy clusters over a range of redshifts is an attractive way to probe fundamental cosmological parameters. Cluster data have been extensively used in the past for this purpose (e.g., Evrard 1989; White et al. 1993; Oukbir & Blanchard 1992; Viana & Liddle 1996, 1999; Eke et al. 1998; Henry 1997, 2000; Viana et al. 2003; Vikhlinin et al. 2003; Voevodkin & Vikhlinin 2004; Schuecker et al. 2003), primarily to constrain the cosmological density parameter. Clusters also can be used as an independent and complementary Dark Energy probe (Starobinsky 1998; Wang & Steinhardt 1998; Huterer & Turner 2001; Haiman et al. 2001; Battye & Weller 2003; Molnar et al. 2004; Hu & Cohn 2006).

These cosmological applications rely on the existence of large, unbiased, and statistically complete cluster samples. Using the X-ray emission of the hot intracluster medium (ICM) is one of the best methods of finding distant clusters (Gioia et al. 1990a; Rosati et al. 1995; Vikhlinin et al. 1998a). A comparison of the efficiency of detecting clusters in X-rays versus other methods can be found, for example, in Rosati et al. (2002). The presently available X-ray selected samples are those from the *Einstein* Extended Medium Sensitivity Survey (EMSS; Gioia et al. 1990b; Stocke et al. 1991) and various samples derived from the *ROSAT* PSPC observations — the 160d survey (Vikhlinin et al. 1998a; Mullis et al. 2003), Bright SHARC (Romer et al. 2000), WARPS (Scharf et al. 1997; Perlman et al. 2002), SHARC South (Burke et al. 2003), NEP (Henry et al. 2001; Gioia et al. 2003), and RDCS (Rosati et al. 1998). There is an ongoing survey based on *ROSAT* HRI data (BMW, Moretti et al. 2004), and also a survey sampling very X-ray luminous clusters using the data from the *ROSAT* All-Sky Survey (Ebeling et al. 2001a, MACS).

The largest sample published to date comes from the 160d survey. In that survey, clusters were serendipitously selected as extended X-ray sources in the inner region of the *ROSAT* PSPC field of view where the angular resolution is sufficient to spatially resolve clusters even at high redshifts. The 160d catalog includes 203 clusters, 43 of them at $z > 0.4$. MACS is expected to find a similar number of distant clusters, all with much higher X-ray luminosities.

None of the previous *ROSAT* surveys based on pointed observations made use of all data suitable for finding distant clusters. Our new survey does exactly that. It is obtained by applying the 160d cluster detection algorithm to virtually all suitable *ROSAT* PSPC fields (1610 in total), resulting in a sky coverage of 397 deg^2. Hereafter, we call it the 400d survey. The 400d sample includes only objects with an observed X-ray flux above 1.4×10^{-13} erg s^{-1} cm^{-2} in the 0.5–2 keV band. This flux limit corresponds to an X-ray luminosity of 1.1×10^{44} erg s^{-1} at $z = 0.5$[6] or temperature $T \approx 5$ keV through the $L_x - T$ relation (Markevitch 1998). Because of the relatively high flux threshold, our catalog does not include low-luminosity systems at $z > 0.3$, nor any clusters at very high redshifts ($z \gtrsim 1$). Instead, it provides a representative snapshot of the population of "typical" clusters at $z = 0.3 - 0.8$. In this Paper, we present the 400d cluster catalog and describe the calibration of the survey's effective area and volume through extensive Monte-Carlo simulations. We also provide updated measurements of the cluster $\log N$–$\log S$ relation and the X-ray luminosity function.

Electronic address: burenin@hea.iki.rssi.ru
[1] Space Research Institute (IKI), Profsoyuznaya 84/32, Moscow, Russia
[2] Harvard-Smithsonian Center for Astrophysics, 60 Garden Street, Cambridge, MA 02138, USA
[3] Danish National Space Center, Juliane Maries Vej 30, Copenhagen 0, DK-2100, Denmark
[4] Institute for Astronomy, University of Hawaii, 2680 Woodlawn Drive, Honolulu, HI 96822, USA
[5] Departamento de Astronomia y Astrofisica, Pontificia Universidad Catolica de Chile, Casilla 306, Santiago, 22, Chile

[6] We compute all distance-dependent quantities assuming $\Omega_M = 0.3$, $\Omega_\Lambda = 0.7$, $h = 0.71$. The luminosities are in the 0.5–2 keV band (source rest frame).

2. X-RAY DATA AND SOURCE DETECTION

The 400d survey is based on the *ROSAT* PSPC pointed observations selected from the archive by the following criteria: 1) Galactic latitude $|b| > 25^\circ$, 2) Galactic absorption $N_H < 10^{21}$ cm^{-2}, 3) total clean exposure $t_{\rm exp} > 1000$ s, and 4) targeted at least 10° away from LMC and SMC. Several pointings were discarded because of the large optical extent of the *ROSAT* targets. Compared to the 160d survey, we used pointings at lower Galactic latitudes and also with shorter exposures and higher N_H. We also included pointed observations of extended targets such as star clusters, normal galaxies, and galaxy clusters at moderate and high redshifts, if the target emission did not affect more than 50% of the area in the inner 17.5′ region; no such pointings were used in the 160d survey. The overall sample quality is not degraded by these additional data because the final catalog uses a relatively high flux threshold, 1.4×10^{-13} erg s^{-1} cm^{-2}.

S. Snowden's software (Snowden et al. 1994) was used to clean the PSPC data from high background intervals and to generate exposure maps. Cluster detection is performed in the hard energy band, 0.6–2 keV (justified in Vikhlinin et al. 1998a). Images from multiple observations of the same target were merged, and fields with a total merged exposure time of $t_{\rm exp} < 1000$ s were discarded. The detection threshold for clusters in the $t_{\rm exp} = 1000$ s fields is $\simeq 3 \times 10^{-13}$ erg s^{-1} cm^{-2}.

The final set contains 1610 fields, including all data from the 160d survey (646 fields[7]) plus 964 additional fields. The exposure time distribution in the 400d and 160d surveys is shown in Fig. 1. The field center coordinates and exposure times are listed in Table 1. For each field, we defined a region affected by either X-ray or optical emission from the target (also given in Table 1) and thus unsuitable for serendipitous cluster detection. These target regions are typically 1′ circles for on-axis, point-like targets. Larger regions were used for extended targets. No such regions were defined for pointings without a declared target — those classified under "extragalactic survey" or used to complete the All-Sky Survey (*ROSAT* sequences rp190xxx).

Extended X-ray sources in the central 17.5′ of the field of view were detected with the 160d analysis pipeline. This algorithm (fully described in Vikhlinin et al. 1998a) is a three-step procedure which includes identification of the candidate sources through the wavelet transform, Maximum Likelihood fitting of the selected sources, and final selection based mainly on the significances of source existence and extent. The only modification we made to the 160d pipeline is to drop the requirement that the cluster core-radius exceeds 1/4 of the PSF FWHM. A closer examination showed that this selection significantly decreased the detection efficiency for clusters with small angular size while most of the associated false detections can be easily identified optically. For the 160d fields, the effect of removing this criterion is to add three clusters (0209−5116, 1338+3851, 1514+3636) and three false detections (0522−3628, 1007+3502, 1428+0106).

We detected 287 extended X-ray sources with fluxes above 1.4×10^{-13} erg s^{-1} cm^{-2}, compared to 116 such sources in the 160d sample. For each source we measure its location and total X-ray flux, and also derive uncertainties on these quantities as described in Vikhlinin et al. (1998a).

[7] The only exception is the pointing towards Arcturus which was included in the 160d survey (it contains the extended source 1415+1906) but discarded here because of the target's optical brightness.

TABLE 1
LIST OF *ROSAT* POINTINGS

α (J2000)	δ	$T_{\rm exp}$, ks	Target region[a] $\Delta\alpha$, $\Delta\delta$, r
00 00 07.2	+29 57 01	3.5	···
00 02 28.8	+31 28 47	14.1	···
00 03 19.2	−35 57 00	8.7	115″, 80″, 355″
00 03 21.5	−26 03 36	38.2	30″, 15″, 50″
00 05 19.2	+05 23 59	7.4	−15″, 15″, 80″

NOTE. — The complete version of this table is in the electronic edition of the Journal. The printed edition contains only a sample.
[a] Defined by offsets from the field center and radius.

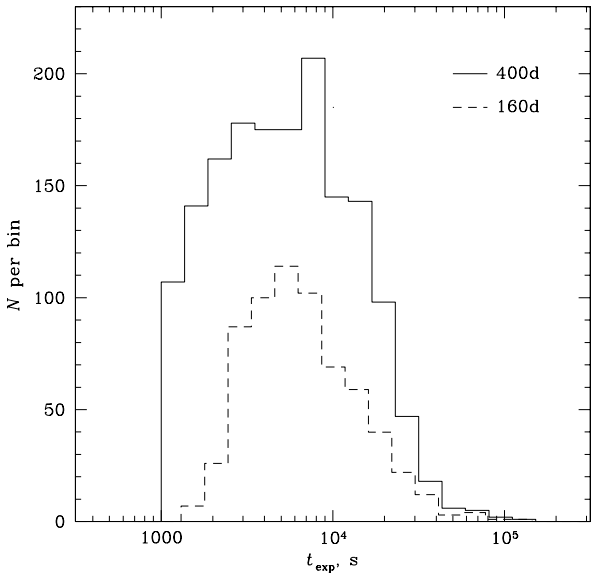

FIG. 1.— Distribution of exposure times in the 400d and 160d surveys.

3. OPTICAL OBSERVATIONS

The X-ray analysis was followed by an extensive optical program whose purpose was to confirm the cluster identifications of our extended X-ray sources, and to measure redshifts of previously unknown clusters. The identification was based on an examination of the optical images of the X-ray candidates. The images were obtained mainly with the Russian-Turkish 1.5-m telescope in the North and with the Danish 1.54-m telescope in the South. The images obtained were sufficiently deep to detect cluster member galaxies out to $z \approx 1$. We considered the X-ray source to be confirmed as a cluster if 1) there was an obvious associated excess in the galaxy number density, or 2) there was a bright elliptical galaxy at the X-ray centroid, even if it was seemingly isolated (this is a signature of so-called fossil groups, see Ponman et al. 1994; Vikhlinin et al. 1999b; Jones et al. 2003). Our cluster identifications are sufficiently reliable even though they do not use spectroscopic redshifts, because extended X-ray emission is by itself a strong indication of a cluster. The cluster identification had to be later revised only for one object (see below). We identified 266 of 287 X-ray candidates as galaxy clusters, groups, or X-ray luminous isolated ellipticals. An additional 5 objects are legitimate extended X-ray sources (e.g., nearby spiral galaxies). Only 16 objects (5% of the sample) remained unidentified; they are most likely false detections (see below). All clusters from the 160d survey with fluxes above our flux limit (116 objects) were re-confirmed in our catalog.

Spectroscopic redshifts for a significant fraction of the 400d clusters were previously known (Table 2). Redshifts for 88

TABLE 2
SUMMARY OF OPTICAL IDENTIFICATIONS

Description	Objects
Detected extended X-ray sources	287
Confirmed clusters, groups, and galaxies	266
Other extended X-ray sources	5
False detections	16
Clusters at target z	24
Clusters in main sample	242
Previously known redshifts	177
Objects present in other catalogs	
160d	116
EMSS	13
WARPS	15
Bright SHARC	22
SHARC South	12
NEP	4
Abell clusters	43
NGC galaxies	10

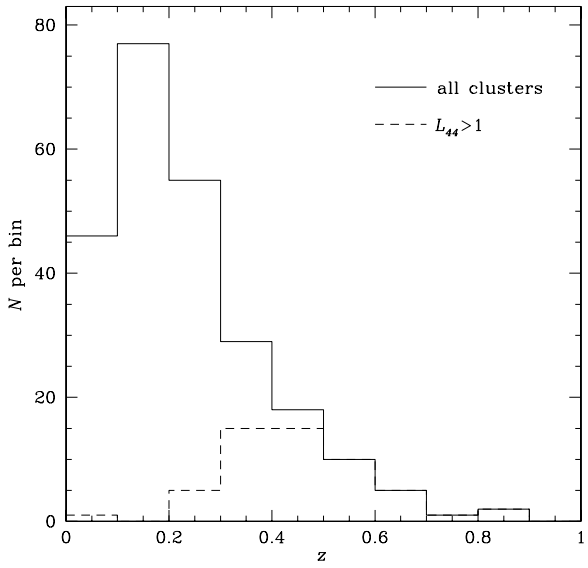

FIG. 2.— Redshift distribution of clusters in the 400d catalog. Dashed histogram shows the higher luminosity clusters, $L_x > 10^{44}$ erg s^{-1}.

clusters were measured in the 160d survey and an additional 27 clusters had known redshifts from other *ROSAT* and *Einstein* surveys: EMSS (Stocke et al. 1991, 8 objects), WARPS (Perlman et al. 2002; Ebeling et al. 2001b, 6 objects), Bright SHARC (Romer et al. 2000, 8 objects), SHARC South (Burke et al. 2003, 1 object), NEP (Gioia et al. 2003, 2 objects), and NORAS (Böhringer et al. 2000, 2 objects). The redshifts for 62 low-z clusters were available from the literature and various public catalogs. The redshifts of the remaining 89 clusters were measured by us with the Keck II, ESO 3.6-m, NTT, Magellan, FLWO 1.5-m, Nordic Optical Telescope, and Danish 1.54-m telescopes (Hornstrup et al., in preparation).

The redshift distribution of the 400d sample is shown in Fig. 2. The median redshift is relatively low, $z = 0.20$, as expected, since all X-ray flux limited samples are dominated by low-luminosity systems at low redshifts. Clusters with higher X-ray luminosities are at higher redshifts on average. For example, the median redshift of clusters with $L > 10^{44}$ erg s^{-1}, is $z = 0.46$ (dashed histogram in Fig. 2). The most distant 400d cluster is ClJ1226+3332 at $z = 0.888$, a system previously discovered in the WARPS survey (Ebeling et al. 2001b).

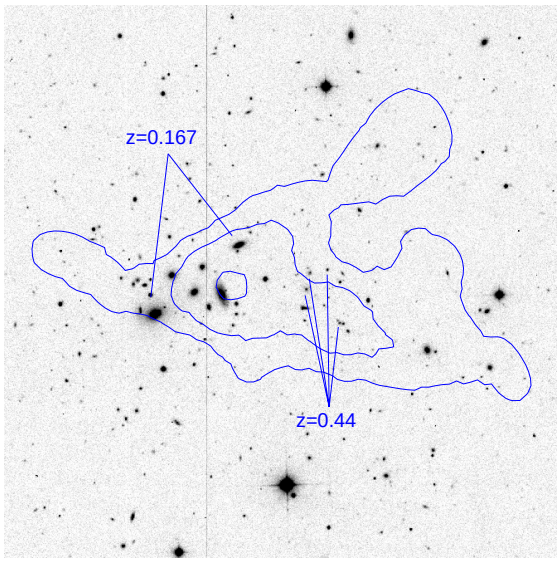

FIG. 3.— R-band image of 0141−3034 with overlaid *ROSAT* contours. North is up and East is to the left.

Sixteen extended X-ray sources did not have any obvious counterparts in the deep optical images. In principle, we cannot exclude that these are very distant clusters ($z > 1$). However, we note that a similar number of *false detections* is expected in our sample because of point source confusion (§ 6.3) and so the unidentified sources are most likely not clusters. To be conservative, however, one should use an upper redshift boundary of $z \approx 1$ for the 400d catalog within which our sample should be essentially complete and clean.

4. THE CATALOG

The 400d object catalog is presented in Tables 4–7. The main cluster list is given in Table 4. The clusters within $|\Delta z| < 0.01$ of the *ROSAT* target redshift are listed separately in Table 5 because they are not entirely serendipitous. Extended non-cluster sources and likely false X-ray detections are listed in Tables 6 and 7, respectively. For each source we provide the coordinates of the X-ray centroid (columns 2–3; a typical positional uncertainty is 10″ – 30″), the total unabsorbed flux in the 0.5–2 keV band (column 4), the redshift (column 5) with reference (column 6), the total X-ray luminosity in the 0.5–2 keV band (column 7), and notes on the optical IDs (column 8). The X-ray luminosity was computed as described in Appendix B.

4.1. *Notes on Individual Objects*

0106+3209 — This source was detected in the EMSS and identified as a QSO at $z = 2.03$. However, this identification is ambiguous (Stocke et al. 1984) because the QSO is projected on a foreground elliptical galaxy. *ROSAT* PSPC data clearly show that the X-ray source is extended, and that a point source at its center cannot contribute more than 10–30% of the total flux. Therefore we identify this object as a galaxy group, a conclusion that is confirmed by a *Chandra* observation of this field (Hardcastle et al. 2002).

0141−3034 — A $z = 0.44$ cluster near the X-ray centroid is projected on the galaxy group AM 0139–305 ($z = 0.17$). Each object is associated with a separate X-ray peak (Fig. 3). The fluxes of these systems cannot be deblended using the *ROSAT* data. We estimate that the foreground group can contribute up to 30% of the total X-ray flux.

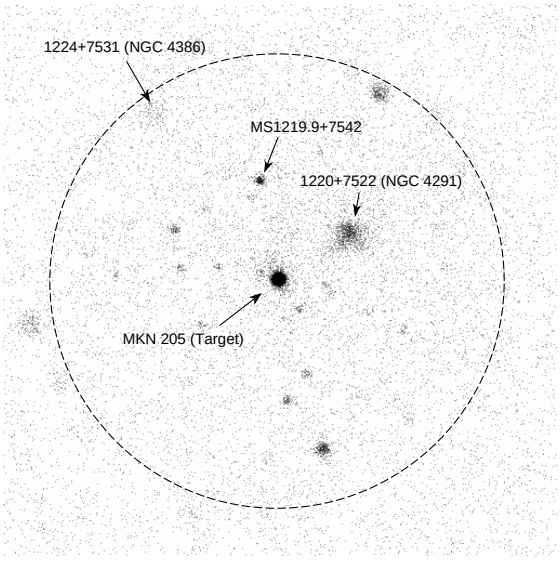

FIG. 4.— *ROSAT* image containing the EMSS source MS1219.9+7542 (= Bright SHARC source RXJ1222.1+7526). The source spatial extent is comparable to that of the *ROSAT* target, MKN 205 (point-like AGN). Therefore, MS1219.9+7542 is clearly dominated by emission from a point source.

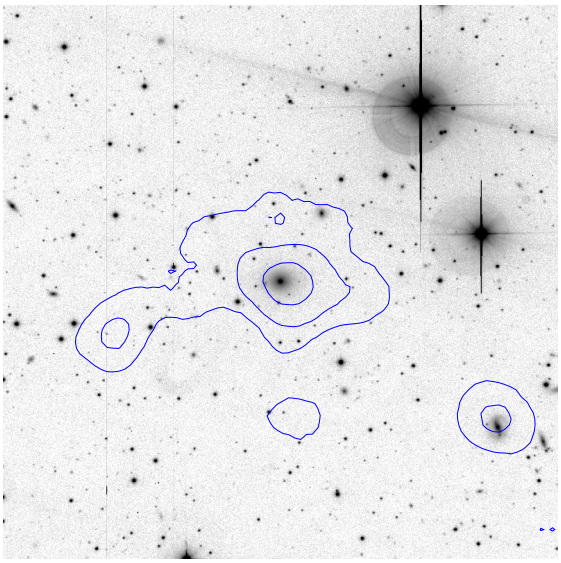

FIG. 5.— R-band image of the 400d cluster 1313−3250 (Bright SHARC object RXJ1313.6−3250) with overlaid *ROSAT* contours.

0350−3801 — The aspect solution for this *ROSAT* observation (sequence rp190505n00) was incorrect (systematically shifted $\approx 5.4'$ to the South–West). We reconstructed the aspect solution by cross-correlating locations of bright X-ray sources in this field with their locations in the overlapping pointings. After this correction, the extended X-ray source is unambiguously identified as a galaxy cluster at $z = 0.36$.

0809+2811 — This object was detected in the EMSS (MS 0806.6+2820) and classified as an AGN at $z = 0.30$. The optical AGN is located $0.6'$ from the *ROSAT* centroid. The source is significantly extended in the *ROSAT* PSPC image, and there is no point source near the AGN location. We instead identify this source as a cluster at $z = 0.399$.

1002+6858 — This object was identified as a QSO in the EMSS (MS 0958.4+6913, $z = 0.93$). In the *ROSAT* data, we detect both the point source associated with the QSO and extended X-ray emission centered $0.9'$ off the QSO. This object is therefore classified as a cluster. The QSO flux was correctly subtracted by our automatic detection software.

1142+1027 — We revise the Bright SHARC identification of this object as A 1356 (Romer et al. 2000). A 1356 is not detected in the *ROSAT* image. Instead, the extended X-ray source is associated with a more distant galaxy group.

1338+3851 — The galaxy near the center of this source is a radio source, 3C 288. The X-ray source extent is significant but we cannot exclude the possibility of considerable contamination by AGN emission.

1500+2244 — This object is a false detection, based on a recent *Chandra* observation.

5. COMPARISON WITH OTHER X-RAY SURVEYS

The 400d fields overlap with those covered by several earlier surveys. A comparison of our catalog with those from these previous studies, provided below, helps to assess any systematic errors in the X-ray cluster selection, optical identifications, and X-ray flux measurements.

EMSS — The angular resolution of the *Einstein* IPC is $\sim 1'$ (Giacconi et al. 1979), which is larger than the angular core-radius of most of the distant clusters. The inability to rely on the X-ray source extent sometimes leads to incorrect identifications. *ROSAT* data clearly show that, of 16 clusters in common between the 400d and EMSS samples, 3 were incorrectly identified with AGNs (0106+3209, 0809+2811, and 1002+6858, see § 4.1), and the fossil group 1159+5531 (Vikhlinin et al. 1999b) was classified as a galaxy with weak emission lines. The area covered by the 400d survey contains 13 EMSS clusters, of which we detect 10. MS1019.0+5139, MS1209.0+3917, and MS1219.9+7542 are not included in our catalog because these sources were not recognized as extended. Examination of the *ROSAT* data confirms that their fluxes are dominated by emission from point X-ray sources (see, e.g., Fig. 4 for MS1219.9+7542).

WARPS — The detection algorithm used in the *WARPS* survey (Scharf et al. 1997) essentially selects X-ray candidates by peak surface brightness, with only a weak reliance on the angular extent. This detection algorithm is very different from ours and therefore the comparison with *WARPS* is particularly useful for assessing the systematics of the X-ray selection. Our survey includes 74 of 80 *ROSAT* PSPC fields used in *WARPS*. In this area, the *WARPS* catalog includes 14 clusters and one normal galaxy above our flux limit. We detected all these objects. For two objects, we measure a lower X-ray flux ($< 1.4 \times 10^{-13}$ erg s^{-1} cm^{-2}) so they are not included in our main catalog. All 15 of our clusters in the overlapping area were also detected by WARPS. We conclude that there is no difference in the source lists and possibly a small difference in the flux measurements, which are not statistical since virtually the same data were used, as is the case also with Bright SHARC and SHARC South.

Bright SHARC — The detection algorithm used in the Bright SHARC survey (Romer et al. 2000) is based on the wavelet analysis at a single angular scale. The Bright SHARC catalog contains 32 clusters in the area covered by 400d, all above our flux limit. Our catalog includes 26 of these objects. Of the remaining 6 objects, RXJ0209.4−1008, RXJ0415.7−5535, RXJ0416.1−5546, RXJ1250.4+2530, and RXJ1349.2−0712 were in fact the observation targets, and RXJ1222.1+7526 (=MS1219.9+7542) is not extended (Fig. 4). The 400d catalog contains 78 clusters in the overlapping area, of which only

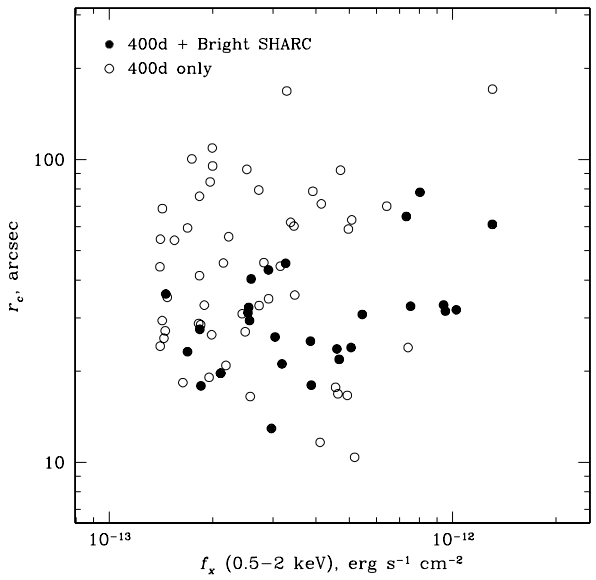

FIG. 6.— The distribution of fluxes and core-radii for the clusters detected in 400d and Bright SHARC surveys in the overlapping area.

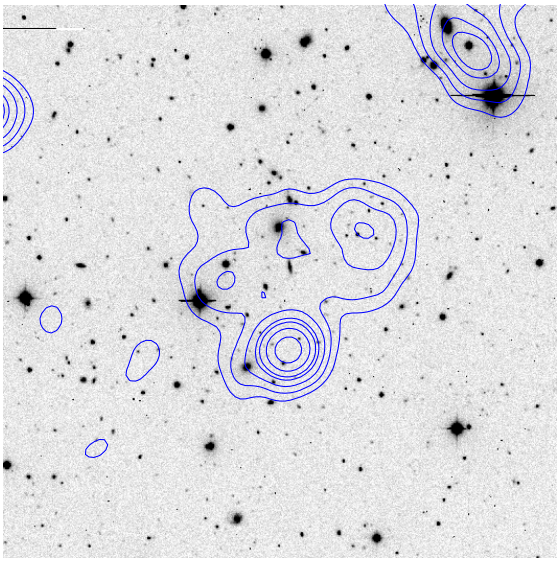

FIG. 7.— R-band image of the 400d cluster 0506−2840 (identified as "multiple point sources" in SHARC South) with overlaid *ROSAT* contours. The point source to the South was correctly removed from the cluster emission.

26 are listed in Bright SHARC. The 400d cluster 1313−3250 was detected (RXJ1313.6−3250) but classified as a "blend". *ROSAT* and optical images, however, support our cluster identification (Fig. 5). Obviously, there are large differences between the Bright SHARC and 400d samples in the overlapping data. We attribute this mostly to the X-ray detection algorithm used in Bright SHARC. This is well illustrated by the comparison of the distributions of cluster fluxes and core-radii in the two surveys (Fig. 6). Obviously, Bright SHARC tends to miss clusters with either large ($r_c \gtrsim 50''$) or small ($r_c \lesssim 20''$) angular extent.

SHARC South— Our survey used 61 of 66 *ROSAT* pointings used in the SHARC South survey (Burke et al. 2003). In these fields, we detect 15 clusters with off-axis angles $> 5'$ (the inner radius used by Burke et al.). All 15 objects were detected in SHARC South but 3 were not optically identified as clusters: 1252−2920 and 2305−3545 were listed as unidentified, and third object, 0506−2840, was listed as "multiple point sources". Inspection of the *ROSAT* image (Fig. 7) shows that there is both a point source (correctly detected in 400d) and an extended X-ray source, clearly associated with a galaxy group. All of the SHARC South clusters above our flux limit are included in the 400d sample. To summarize, SHARC South and our survey have nearly identical X-ray source lists and the difference is in the optical identifications.

NEP— The North Ecliptic Pole (NEP) survey (Henry et al. 2001; Gioia et al. 2003) includes sources in the high-exposure region of the *ROSAT* All-Sky Survey. The nominal detection threshold of the NEP survey is below our flux limit. The advantage of NEP is a large contiguous area (81 deg^2) with fairly uniform X-ray data. The disadvantage for cluster detection is the poor angular resolution, $\approx 2'$ (Boese 2000), which complicated the determination of the spatial extent of detected sources. The total overlap between the 400d and NEP surveys is ≈ 5.8 deg^2, where we detect 6 clusters of which 4 are also listed in the NEP catalog. Our clusters 1746+6848 and 1807+6946 were missed by the NEP probably because of the presence of bright point X-ray sources in their vicinity. There are 13 NEP clusters in the overlapping region, of which we do not detect 8: five appear point-like (Fig. 8), while 3 have fluxes which are too faint for the pointed observations.

Comparison of our cluster list with the overlapping data from other X-ray surveys generally shows good agreement between the catalogs and thus demonstrates robustness of the X-ray cluster selection. In cases where a disagreement is found the cause is not related to the X-ray or optical analysis in the 400d sample. Most of the discrepancies can be traced to errors in the optical identifications, and therefore the role of optical data in the cluster selection should be minimized. The misclassification rate in the NEP and EMSS surveys is relatively high by modern standards. This underscores the need for X-ray telescopes with adequate angular resolution in implementing efficient distant cluster surveys. Robust X-ray analysis techniques applied to such surveys can provide high-quality cluster samples.

6. STATISTICAL CALIBRATION OF THE X-RAY DETECTION ALGORITHM

The X-ray detection procedure of the 400d survey was extensively calibrated. Our approach is similar to that used in the 160d survey (Vikhlinin et al. 1998a). It is based on Monte-Carlo simulations which provide the probability of detecting clusters with given X-ray flux and size, the bias and scatter in the X-ray flux measurements, and the expected number of false detections. We also studied more subtle effects, e.g., how the cluster detectability is affected by substructure in the ICM, or by the presence of central X-ray surface brightness peaks as well as intracluster point sources.

The cluster detectability depends on the observation exposure, the object off-axis distance, the proximity to other sources, and more weakly on secondary effects such as the Galactic absorption and the level of diffuse X-ray background in the field. To properly treat all these effects, we performed simulations in which clusters with different input parameters were placed at random in the real *ROSAT* images. The simulated data were then run through the complete X-ray analysis pipeline. All statistical properties of the 400d survey are obtained from comparison of the measured properties and input parameters for the simulated clusters.

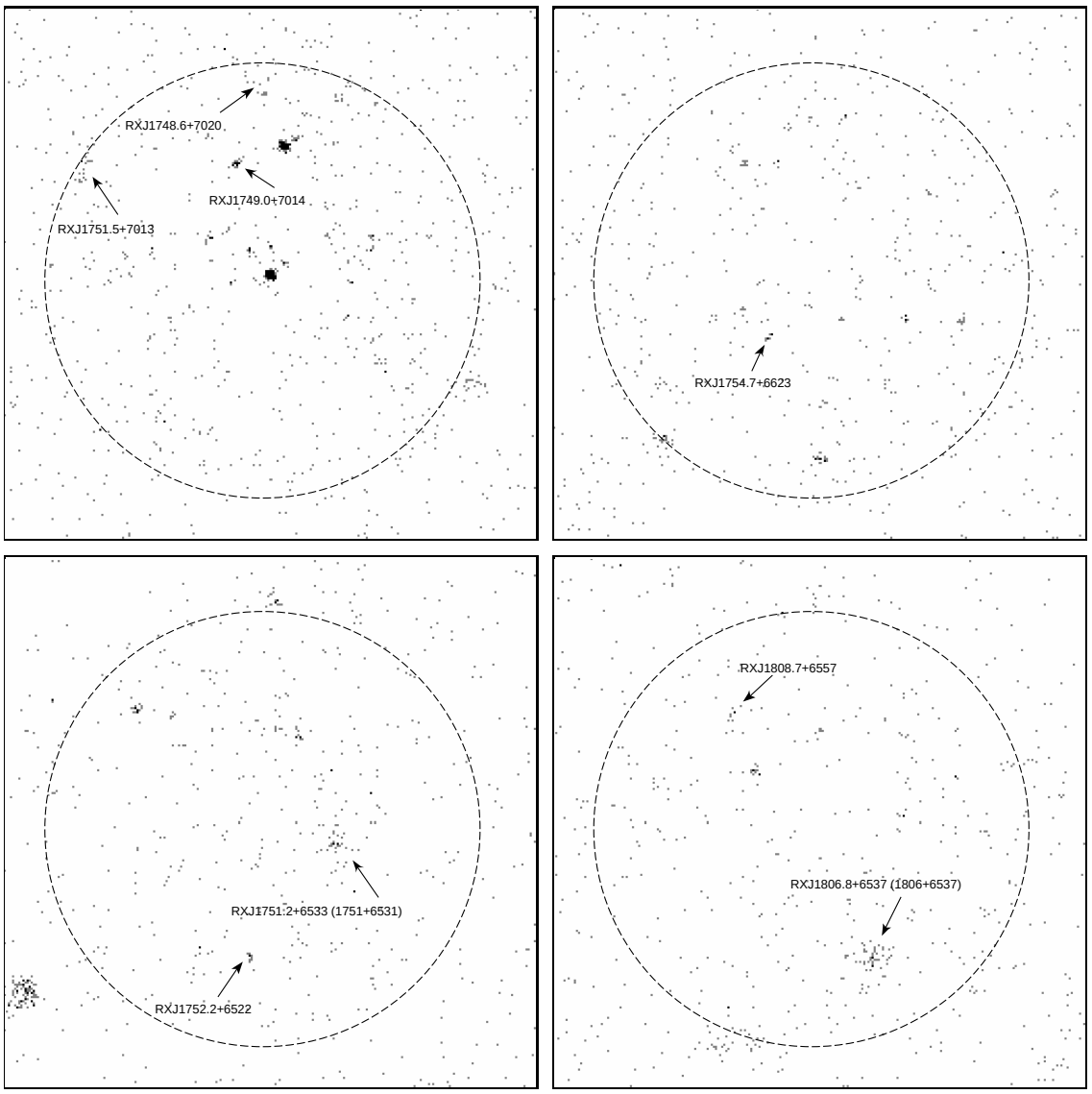

FIG. 8.— Pointed *ROSAT* PSPC observations containing NEP sources RXJ1749.0+7014, RXJ1751.5+7013, RXJ1752.2+6522, RXJ1754.7+6623, and RXJ1808.7+6557 which appear point-like. Also marked are the NEP sources RXJ1748.6+7020 (too faint to be detected in the pointed observation), and RXJ1751.2+6533 and RXJ1806.8+6537 that correspond to our clusters 1751+6531 and 1806+6537. Dashed circles show the central 17.5′ of the FOV.

The input clusters in the majority of the simulations were represented by the elliptical β-models (see Appendix B for details) but more complicated cases were also considered (§ 7.1.1). Input values for fluxes and core radii were selected on a grid spanning the range $10^{-14} < f_x < 3 \times 10^{-12}$ erg s^{-1} cm^{-2} and $5'' < r_c < 300''$. Simulated clusters were placed in randomly chosen survey fields and randomly positioned within the central 18.5′ of the field. This radius is larger than the maximum off-axis angle for detected clusters, 17.5′. This allows us to properly treat edge effects but results in detection probabilities < 1 even for very bright objects. In total, we simulated 1,500,000 clusters.

6.1. *Detection Probability*

The derived probability of cluster detection as a function of flux and core radius is shown in Fig. 9. The probability is normalized to the ratio of input and nominal survey areas (see above) to remove the trivial geometric effects. As expected, the detection probability is nearly 1 for high-flux clusters and decreases at lower f_x primarily because faint clusters are not detected in lower exposure fields. The detection probability for $f_x = 1.4 \times 10^{-13}$ erg s^{-1} cm^{-2}, the 400d catalog flux limit, exceeds 0.5 in a large range of angular core-radii.

At a fixed flux, the detection probability peaks in the core-radius range $r_c = 10'' - 100''$. The probability decreases at large r_c because very extended clusters have a lower ratio of the source and background flux and hence a lower detection significance. The detection probability is small for compact clusters, $r_c < 10''$, because such clusters are more difficult to distinguish from the point sources in the off-axis regions of the field of view (the PSF size changes from 25″ FVWM on-axis to 60″ at an off-axis distance of 17.5′). We note that the detection probability is a much stronger function of X-ray flux than of angular size. In fact, the probability is non-negligible even for very compact clusters, $r_c \approx 5''$. Such objects can still be identified as extended sources because their surface brightness profiles have power-law wings unlike the PSF.

The core radius range within which our detection algorithm is sensitive, 10″–100″, matches well the typical sizes of high-redshift clusters. For example, this corresponds to a range of

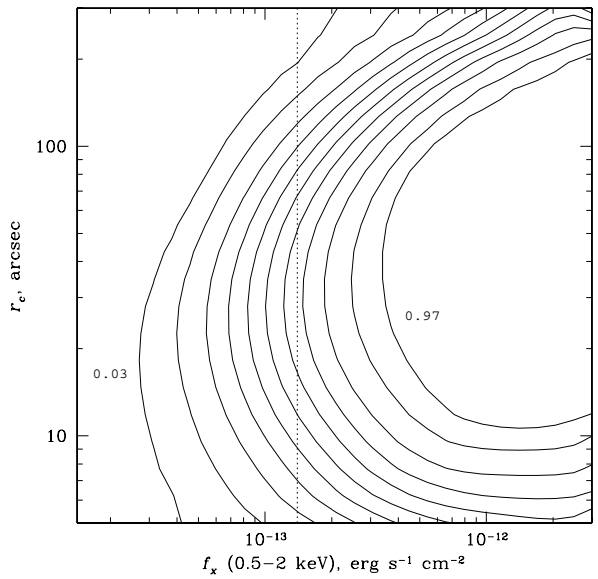

FIG. 9.— Cluster detection probability as a function of input flux and angular core-radius. The contours represent probabilities of 0.03, 0.1, 0.2, 0.3, 0.4, ..., 0.9, and 0.97. Note that this probability does not include the effect of imposing the minimum flux requirement ($f_{\rm min} = 1.4 \times 10^{-13}$ erg s^{-1} cm^{-2}, dotted line) for the clusters to enter our final catalog.

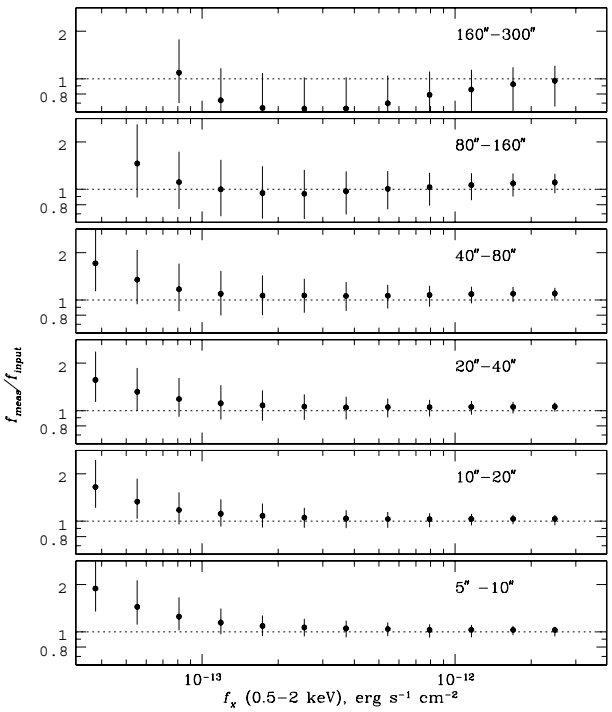

FIG. 10.— Bias and scatter of the flux measurement as a function of input flux. The average value of $f_{\rm meas}/f_{\rm input}$ is shown by points and the rms scatter is indicated by error bars. Each panel corresponds to different ranges of input core-radii, $5'' - 10''$, $10'' - 20''$, ..., $160'' - 300''$.

60–600 kpc at $z = 0.5$. This range compares well with the observed core radii for X-ray luminous clusters which have the median $r_c = 180$ kpc and are distributed in the range 70–350 kpc at both $z \approx 0$ (Jones & Forman 1999) and $z \approx 0.5$ (Vikhlinin et al. 1998b). Even at $z = 1$, an angular size of $10''$ corresponds to a physical radius of 80 kpc, which is near the lower boundary of the observed core-radius distribution.

6.2. *Bias and Scatter in the Flux Measurements*

Figure 10 shows the average bias and scatter in the flux measurements for detected clusters of different angular size. There is no significant bias at fluxes $f_x > 1.4 \times 10^{-13}$ erg s^{-1} cm^{-2}, except for $r_c > 160''$ where the measured f_x are biased low because the local background is overestimated. This effect is strong only at low redshifts. For example, the largest core radius in the Jones & Forman (1999) sample is $r_c = 350$ kpc, corresponding to an angular size of $r_c < 100''$ at $z > 0.2$. Fluxes of faint clusters are systematically overestimated which is a typical example of Malmquist bias. This problem is confined to the flux range below the limiting flux of our catalog.

Our simulations provide also the shape of the $f_{\rm meas}/f_{\rm input}$ distribution. The knowledge of this distribution is required, e.g., for accurate calculations of the survey area or volume for clusters near our flux limit. An example of the flux scatter distribution derived from the simulations is shown in Fig. 11. The scatter distribution can be approximated by a log-normal function (dotted line). However, there is no need to use this approximation because the distribution is sampled sufficiently accurately except for the extreme $\sim 1\%$ upper and lower tails.

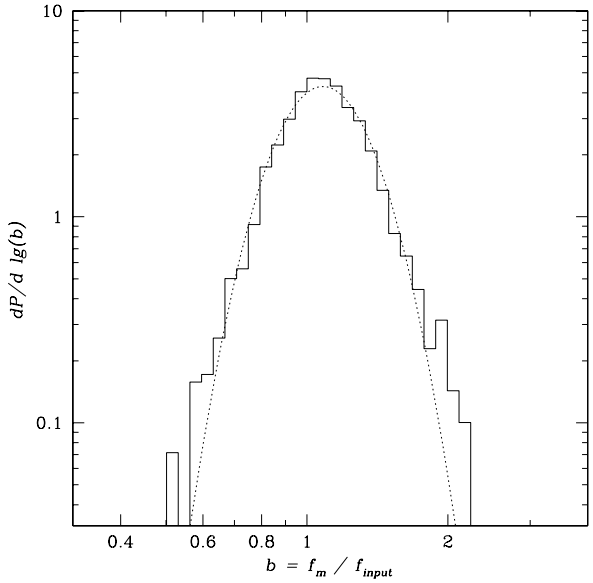

FIG. 11.— The distribution of scatter in the flux measurements for simulated clusters with $f_x = (1.4 - 2) \times 10^{-13}$ erg s^{-1} cm^{-2} and $r_c = 20'' - 35''$. The dotted line shows the log-normal approximation.

6.3. *False Detections*

As mentioned above, the 400d catalog contains 16 unidentified sources. They are most likely false X-ray detections arising from confusion of point sources. We identified most such cases through deep optical imaging (§ 3). However, it is useful to estimate the false detection rate independently from the optical data, to make sure that we are not missing a new interesting class of sources (e.g. clusters at very high redshift). Our approach is identical to that used for the 160d survey. We simulated *ROSAT* PSPC images containing only point sources and the diffuse background. The source fluxes were derived from the observed $\log N$–$\log S$ relation (Hasinger et al. 1993) and their locations were chosen either randomly or according to the angular correlation function from Vikhlinin & Forman (1995). The resulting images correctly reproduce the fluxes and spatial distribution of detectable sources as well as the background fluctuations caused by undetected sources.

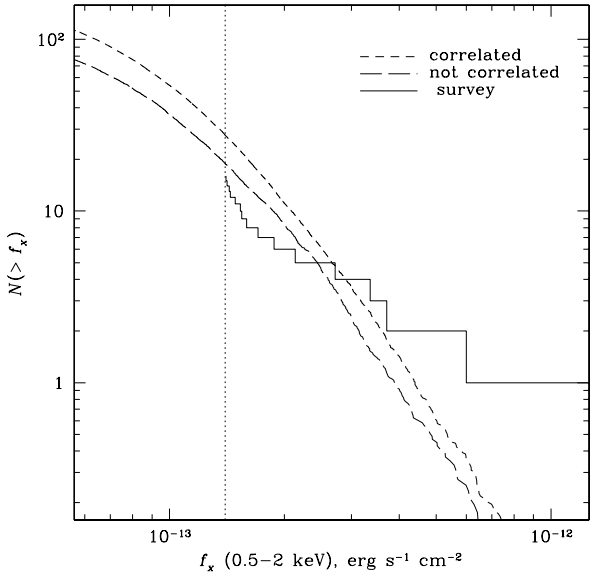

FIG. 12.— The flux distributions for unidentified 400d sources (histogram) and false detections derived in the simulations with randomly distributed (long-dashed line) and correlated (short-dashed line) point sources.

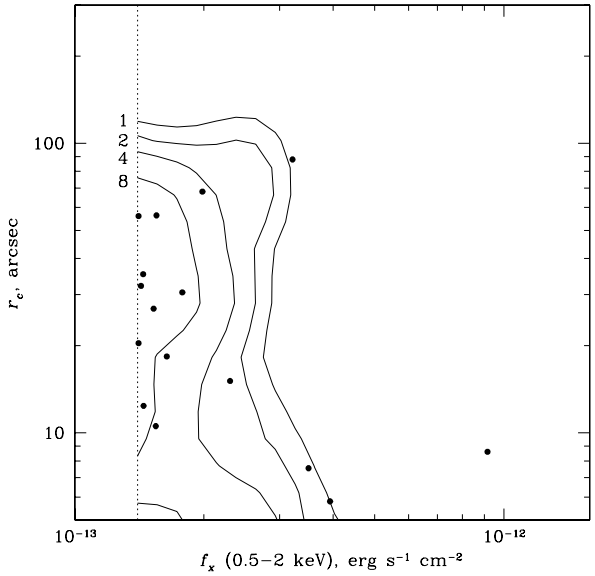

FIG. 13.— The flux vs. size distribution of false detections. The isodensity levels are shown by contours labeled to indicate how many false sources are outside the contour. The points show unidentified 400d sources.

All extended sources detected in these simulations are false by design. The distributions of their fluxes and sizes are shown in Fig. 12 and 13. The total number of unidentified sources in the 400d catalog (16) is consistent with the number of false detections expected for randomly distributed point sources (18.6). It is smaller than, but marginally consistent with, 27.1 false detections expected for correlated point sources. We note that the angular correlation amplitude measured by Vikhlinin & Forman (1995) for point sources with $f \gtrsim 10^{-14}$ erg s^{-1} cm^{-2} is not necessarily directly applicable in the flux range of sources mostly responsible for false detections in the 400d sample, $f \gtrsim 10^{-13}$ erg s^{-1} cm^{-2}. The distributions of fluxes and radii for unidentified sources and false detection also match very well (Fig. 13). Given the good agreement in the number and properties of unidentified 400d sources and false detections in the simulations, we conclude that the unidentified sources are most likely not clusters.

6.4. *Effects of Point Sources Near Cluster Centers*

In some low-redshift clusters there are X-ray bright AGNs associated with the central cluster galaxies (Crawford & Fabian 2003). The X-ray luminosity of the central AGN is typically much lower than that of the host cluster. However, the AGN fraction as well as their typical X-ray luminosities can increase at high redshift. Our analysis software does not attempt to subtract the contribution of point sources near the center (within ≈ 1 FWHM of the PSF) from the cluster flux. This is a deliberate decision to avoid that the peaked X-ray emission from the cluster cooling cores is misinterpreted as the signature of a central AGN. Also, deblending of the central AGNs is an ill-posed problem in general because the angular size of high-redshift clusters is close to the PSF width. The effect of central point sources is twofold. First, they increase the source detectability but decrease our ability to identify it as extended. Second, the cluster flux is biased high if the point source emission is not subtracted. These effects were studied through additional Monte-Carlo simulations.

First, we note that our main simulations already include the effects associated with the chance projection of background sources. Also, individually detectable point sources are automatically removed from the cluster flux if they are located outside the central region (e.g., Fig.7). Therefore, we consider here only sources located within the cluster core radius. The simulations proceed as usual but we place point sources of various flux on top of input β-model clusters. Point sources were placed either at the center of the β-model (to simulate AGNs in central galaxies of relaxed clusters) or randomly distributed within a $1\,r_c$ circle (to simulate AGNs in non-central galaxies or merging clusters).

Figure 14 shows the effect of central point sources on the detection probability for clusters with fluxes near our catalog threshold ($f_{\rm ext} = (1.4-3)\times 10^{-13}$ erg s^{-1} cm^{-2}). The curves show the detection probability as a function of the ratio $f_{\rm point}/(f_{\rm ext}+f_{\rm point})$. The average detection probability for clusters without central sources is shown by the horizontal line. The detection probability decreases significantly only for $f_{\rm point} > 0.5$ (i.e., the point source is more luminous than the host cluster). Even though the detection probability is affected weakly, the measured flux is always strongly biased (Fig.15). We measure essentially $f_{\rm ext}+f_{\rm point}$, except in a small number of cases when our algorithm enters the deblending mode and $f_{\rm ext}$ is correctly recovered.

To summarize, the presence of X-ray bright central AGNs should not affect the catalog completeness unless the AGN luminosities exceed those of the host clusters, $\sim 10^{44}$ erg s^{-1} at $z = 0.5$. However, the *ROSAT* X-ray fluxes can be overestimated in such cases. *Chandra* observations of our distant clusters will help to assess the importance of this effect.

7. USING THE SURVEY STATISTICAL CALIBRATION

The most general way to fit models of the cluster population to the 400d data is through the detection probability and flux measurement scatter functions derived above. The predicted "response" of the 400d survey to clusters with a distribution of fluxes and sizes $n(f, r_c, z)$ is

$$n_{\rm obs}(f_m, z) = \iint P_m(f_m|f, r_c) P_d(f, r_c)\, n(f, r_c, z)\, dr_c\, df, \quad (1)$$

where f_m is the measured flux, $P_d(f, r_c)$ is the detection probability, and $P_m(f_m|f, r_c)$ is the scatter in the flux measurement

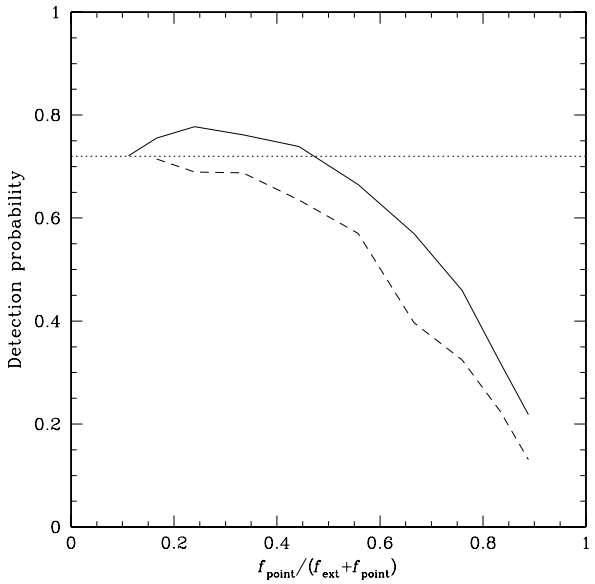

FIG. 14.— Detection probability for simulated clusters with point sources near the center, as a function of the point-source flux fraction. The extended component has $f = (1.4-3)\times10^{-13}$ erg s^{-1} cm^{-2} and $r_c = 10''-60''$. The horizontal line shows the mean detection probability for such clusters without the point sources. Dashed and solid lines show the cases of point sources located within 15″ and 1 r_c from the cluster center, respectively.

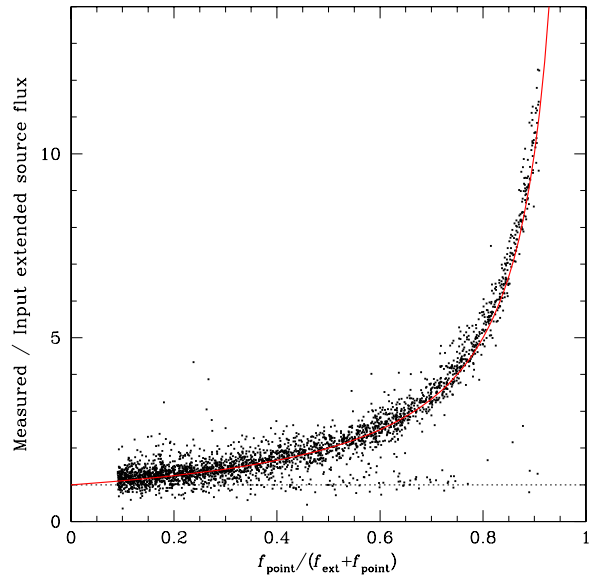

FIG. 15.— Bias in the flux measurements caused by point sources. The solid line shows the expected bias in the case when the point source flux is simply added to the cluster, $(f_{point}+f_{ext})/f_{ext}$.

as a function of true flux and size. The function $n_{obs}(f_m, z)$ is used to compute the likelihood given the number of actually observed clusters. However, it is useful also to have simpler functions such as the sky coverage or the survey volume as a function of cluster luminosity. Below, we demonstrate how such functions can be computed and used for non-parametric derivations of the cluster $\log N - \log S$ distribution or the X-ray luminosity function.

7.1. *Efficiency of Selection to 400d Catalog*

The 400d catalog includes only clusters with a measured flux above 1.4×10^{-13} erg s^{-1} cm^{-2}, i.e. we discard objects with fainter fluxes even if they pass the detection significance

TABLE 3
EFFECTIVE SKY COVERAGE OF THE 400D CATALOG

f_x, (erg s^{-1} cm^{-2})	$AP_{sel}(f)$	$AP_{sel}(f,z)$ $z=0.3$	$z=0.5$	$z=0.8$
4.0×10^{-14}	1.0	1.1	1.2	1.1
6.0×10^{-14}	4.5	4.8	4.7	4.7
8.0×10^{-14}	13.5	14.6	15.0	14.9
9.0×10^{-14}	20.3	21.7	21.6	21.8
1.0×10^{-13}	32.7	34.2	33.9	34.3
1.1×10^{-13}	51.0	52.2	51.4	52.2
1.2×10^{-13}	76.0	77.3	76.2	77.6
1.3×10^{-13}	108.6	109.0	108.1	109.8
1.4×10^{-13}	145.3	143.0	142.2	146.0
1.5×10^{-13}	177.6	172.5	173.2	177.9
1.6×10^{-13}	207.5	201.7	203.6	208.4
1.7×10^{-13}	230.1	222.6	226.8	231.7
1.8×10^{-13}	248.2	240.5	245.8	250.2
2.0×10^{-13}	278.8	270.7	278.1	281.1
2.4×10^{-13}	313.6	303.6	314.4	315.9
3.0×10^{-13}	340.6	333.4	342.7	342.7
4.0×10^{-13}	366.0	364.0	368.8	367.0
5.0×10^{-13}	378.9	379.7	382.5	380.1
7.0×10^{-13}	384.2	388.9	390.7	388.3
1.0×10^{-12}	388.9	395.4	394.9	392.4

NOTE. — The table lists effective sky coverage (in units of deg^2) of the 400d catalog as a function of true cluster flux. The coverage is the product of the selection probability (§ 7.1) and geometric survey area, 446.3 deg^2. Column 2 gives the area averaged over all redshifts (eq.4) and columns 3–5 give more accurate averages for clusters at $z = 0.3$, 0.5, and 0.8 (eq.3).

criteria. The probability for a cluster to be selected in the catalog can be computed as

$$P_{sel}(f, r_c) = P_d(f, r_c)\int_{f_{min}}^{\infty} P_m(f_m|f, r_c)\, df_m \qquad (2)$$

where f_{min} is the minimum flux required for the cluster selection ($f_{min} = 1.4\times10^{-13}$ erg s^{-1} cm^{-2} for the main 400d catalog, or a higher value if the probability is computed for a brighter subsample). Note that $P_{sel}(f, r_c)$ is different from the detection efficiency $P_d(f, r_c)$.

In practice, $P_d(f, r_c)$ and $P_m(f_m|f, r_c)$ are weak functions of r_c in the plausible range of angular sizes of distant clusters. This allows us to eliminate the r_c-dependence by averaging eq.(2) with a realistic distribution of core radii[8], $n(f, r_c, z)$:

$$P_{sel}(f, z) = \frac{\int P_{sel}(f, r_c)\, n(f, r_c, z)\, dr_c}{\int n(f, r_c, z)\, dr_c}. \qquad (3)$$

The z-dependence in eq.(3) arises because the X-ray analysis depends on the angular, not proper size. A further simplification is to use a realistic model for the cluster distribution as a function of flux and z[9] and average over z:

$$P_{sel}(f) = \frac{\iint P_{sel}(f, r_c)\, n(f, r_c, z)\, dr_c dz}{\iint n(f, r_c, z)\, dr_c\, dz} \qquad (4)$$

The probabilities in eq.(2), (3), and (4), multiplied by the geometric area of the 400d survey, give (in the decreasing order of accuracy) the effective sky coverage of the 400d catalog as a function of *true* flux. The calculations for our reference cluster population model (Appendix B) are shown in Fig.16 and tabulated in Table 3.

[8] We use the measurements by Jones & Forman (1999), see Appendix B.
[9] Such a distribution can be computed using a model for the X-ray luminosity function, see Appendix B

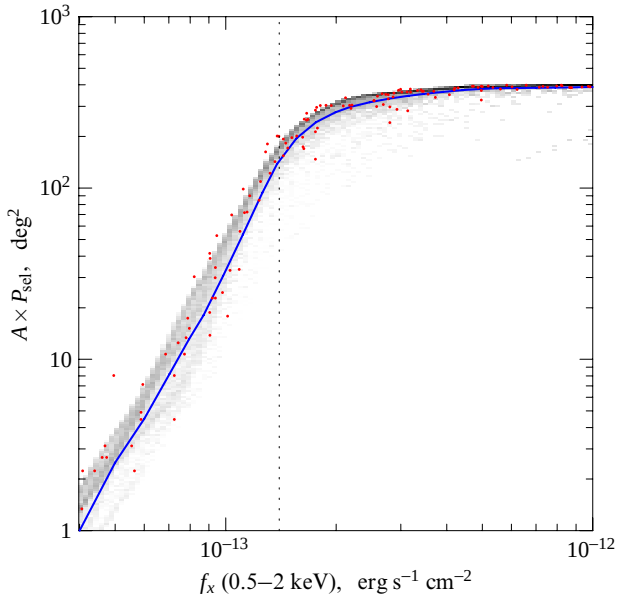

FIG. 16.— Selection efficiency as a function of flux (solid line; numerical values are given in the second column of Table 3). Selection efficiencies for clusters with X-ray morphologies from the $z \sim 0$ sample (§7.1.1) are shown by points. They agree very well with the efficiencies for β-model clusters drawn from our reference population model (shown by shading). The mean of the distribution at each flux (represented by the line) is offset from the peak (densest shading) because of a long tail towards lower efficiencies. This tail is present both in the β-model clusters and those from the real population.

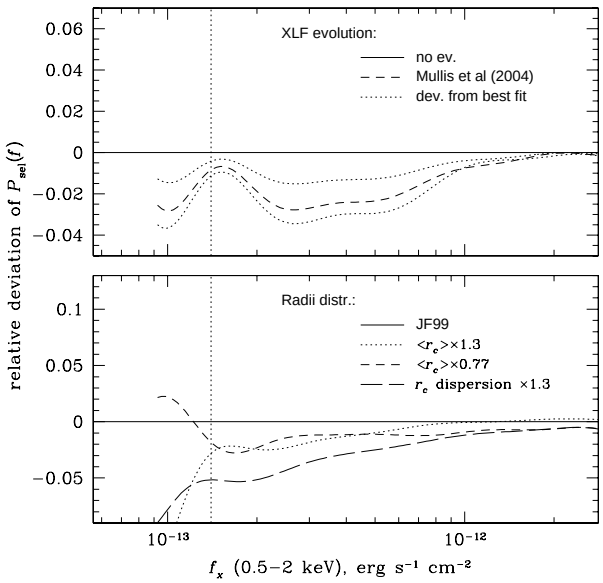

FIG. 17.— Sensitivity of the survey area calculations to the XLF evolution (top) and distributions of core-radii (bottom). In the top panel, we compare the selection probabilities calculated assuming non-evolving XLF and the best-fit model from Mullis et al. (2004, dashed line). The range of $P_{\rm sel}(f)$ corresponding to the measurement uncertainties in the Mullis et al. is shown by dashed lines. The bottom panel illustrates the sensitivity of $P_{\rm sel}(f)$ to variations of the mean and width of the core radius distribution by ±30%.

7.1.1. *Sensitivity to the Cluster Population Models*

The calculation of the cluster selection probability (eq. 3, 4) in principle depends on the exact form of the core-radius distribution and also on the luminosity function and its evolution. However, these dependencies are weak as shown below.

Figure 17 shows the relative deviations of $P_{\rm sel}(f)$ (eq.4) calculated with different models of the cluster X-ray luminosity function (XLF) and core-radius distribution. The top panel demonstrates the sensitivity to the assumed evolution of the XLF (this affects the z-distribution of clusters with given X-ray flux and hence their angular core-radii). $P_{\rm sel}(f)$ changes by less than ±2% in the full range of the XLF evolution models consistent with the Mullis et al. (2004) measurements. $P_{\rm sel}(f)$ is slightly more sensitive to the assumed distribution of core radii (bottom panel in Fig.17). For example, if the average core radius for distant clusters is scaled by factors 1.3 and 0.77 relative to the non-evolving Jones & Forman (1999) distribution, $P_{\rm sel}(f)$ decreases by 3%. Such an evolution of the average core radius is inconsistent with observations (Vikhlinin et al. 1998b).

All the cases considered in Fig.17 still assume that the cluster emission follows elliptical β-models. What if we consider a more realistic range of cluster structures, from peaked cooling cores to strong mergers? To check this, we used a complete flux-limited sample of 38 clusters ($f_x > 1.4 \times 10^{-11}$ erg s^{-1} cm^{-2}) in the redshift range $0.03 < z < 0.1$ from the HIFLUGCS catalog (Reiprich & Böhringer 2002). The minimum luminosity in this sample of low-redshift clusters approximately corresponds to the 400d sensitivity limit at $z = 0.35$. These clusters show a wide range of morphologies and represent an unbiased (with respect to structure) snapshot of the local population (Fig.18). Template images created from *ROSAT* and *Chandra* observations of these clusters (shown in Fig.18) were used in the simulations instead of the elliptical β-models. Each cluster was put at $z = 0.35$, 0.45, 0.55, and 0.80. We scaled the templates in flux and angular size according to the distance to these redshifts but kept the X-ray luminosity and physical size of each cluster constant. Constant luminosity corresponds to a weakly X-ray luminosity function, approximately as observed (Mullis et al. 2004). Constant size corresponds approximately to a non-evolving scale radius in the Navarro, Frenk & White model (Navarro et al. 1997) of the total mass density profile, as is indeed expected (Bullock et al. 2001).

Each cluster leaves a track in the $P_{\rm sel}(f)$ plot when its redshift is varied. The combined results for all clusters are shown by points in Fig.16. There is a very good agreement with the calculations using β-model clusters from our reference model. We conclude that the deviations of the cluster X-ray morphologies from the β-model do not play a significant role in the 400d survey selection functions.

7.2. *Cluster* $\log N - \log S$.

If the fluxes of all clusters were measured precisely, the $\log N - \log S$ could be computed using $P_{\rm sel}(f)$ from eq.(4),

$$N(>f) = \sum_{f_i > f} (A\, P_{\rm sel}(f_i))^{-1} \qquad (5)$$

where f_i is the X-ray flux of individual detected clusters and A is the geometric survey area. However, because of the flux measurement errors, the $\log N - \log S$ estimated by eq.(5) will be biased (Eddington bias, Eddington 1940). Kenter & Murray (2003) discuss how to reconstruct the true $\log N - \log S$ function by fitting an analytic model to the distribution of measured object fluxes. However, it is also useful to reconstruct the true $\log N - \log S$ non-parametrically. A possible approach (Vikhlinin et al. 1998a) is to define the effective sky coverage as a ratio of differential $\log N - \log S$ for detected and input sources from a realistic input population (e.g. a power law with Euclidean slope). This ratio is usually insensitive to the exact form of the input population and therefore can

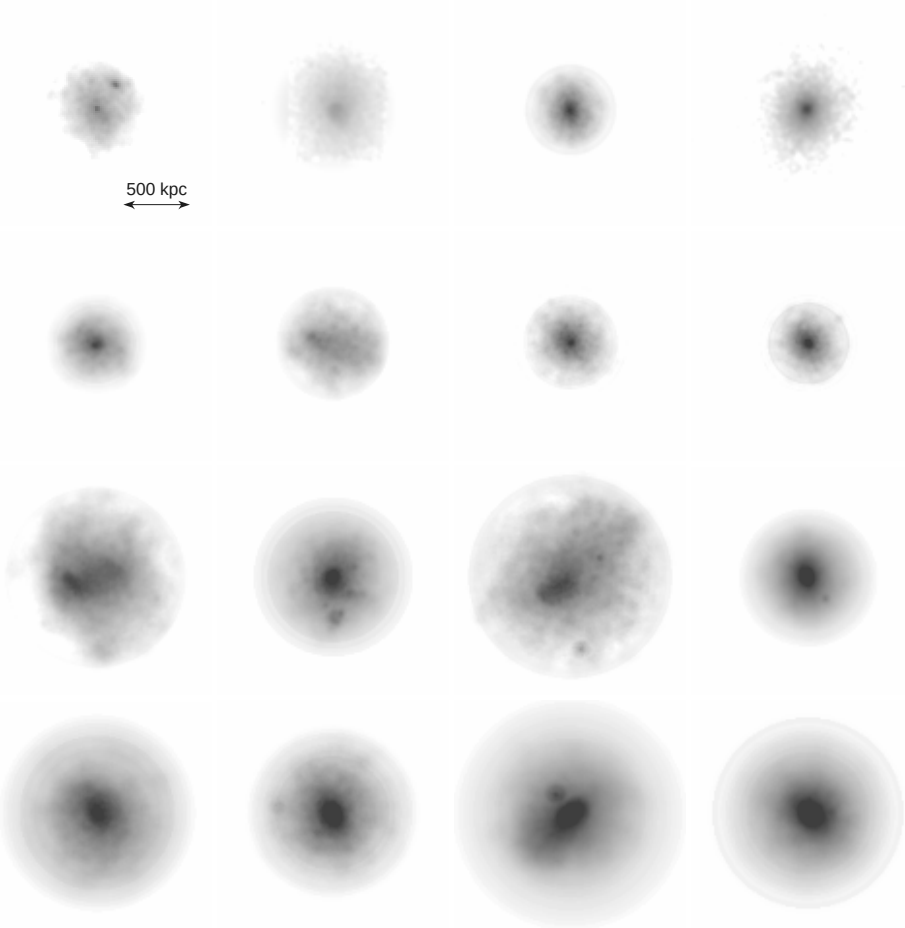

FIG. 18.— Sample images of low-z clusters used in the simulations described in § 7.1.1. From left to right and top to bottom, the adaptively smoothed images are for A2634, A0576, A2589, EXO0422, A2657, A3376, A2063, A2052, A0754, A0085, A3667, A1795, A0401, A2029, A2142, and A0478. The images are scaled to the same physical size.

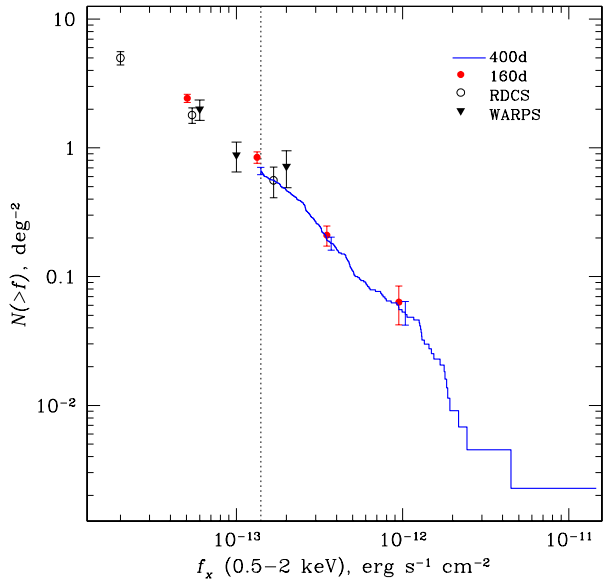

FIG. 19.— The $\log N - \log S$ function for the 400d cluster sample (solid histogram; error bars indicate statistical uncertainties at several flux thresholds). The results from earlier surveys (160d, Vikhlinin et al. 1998a; RDCS, Rosati et al. 1998; WARPS, Jones et al. 1998) are shown by points with error bars.

be used for non-parametric $\log N - \log S$ reconstruction. The corresponding calculation follows from eq.(1):

$$A_{\rm eff}(f_m) = A\frac{\iiint P_m(f_m|f,r_c)\,P_d(f,r_c)\,n(f,r_c,z)\,dr_c\,df\,dz}{\iint n(f_m,r_c,z)\,dr_c\,dz}, \quad (6)$$

where $n(f,r_c,z)$ is the reference cluster population model (Appendix B). The cluster $\log N - \log S$ is then estimated as

$$N(>f) = \sum_{f_i>f}(A_{\rm eff}(f_i))^{-1}. \quad (7)$$

The results are shown in Fig.19 in comparison with several earlier surveys. There is very good agreement in the overlapping flux range. Note a marginal deficit of very bright clusters, $f_x > 3\times10^{-12}$ erg s^{-1} cm^{-2}, in our sample relative to a power law extrapolation from fainter fluxes. This might be related to the fact that many of the high-flux clusters were previously known and used as targets for *ROSAT* pointings. However, this deficit is marginal. The observed $\log N - \log S$ distribution is in fact consistent with a single power law throughout our flux range, $N(>S) = K\,(S/1.4\times10^{-13})^{-\gamma}$ where $\gamma = -1.25\pm0.07$ and $K = 0.66\pm0.03$ per square degree.

7.3. *Survey Volume and X-ray Luminosity Function*

The area calculations discussed in §§ 7.1 and 7.2 are straightforwardly generalized for computations of the search volume. For example, the comoving search volume for clus-

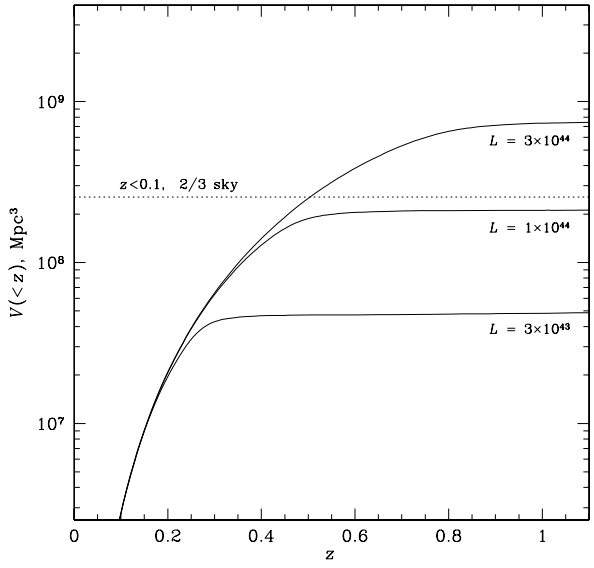

FIG. 20.— The volume covered by the 400d survey within redshift z, for three X-ray luminosities, $L_x = 3\times10^{43}$, 10^{44}, and 3×10^{44} erg s^{-1}. The volumes are calculated from eq.(8) where $z_1 = 0$. For reference, the horizontal line shows the typical volume covered at low redshifts by the *ROSAT* All-Sky Survey cluster samples (excluding the region near the Galactic plane).

ters with *true* luminosity L in the redshift interval $z_1 - z_2$ is

$$V(L) = A \int_{z_1}^{z_2} P_{\rm sel}(f,z)\,\frac{dV}{dz}\,dz, \qquad (8)$$

where dV/dz is the cosmological comoving volume per redshift interval and $P_{\rm sel}(f,z)$ is given by eq.(3). The flux and luminosity in eq.(8) are related through eq.(B2) in Appendix B. In Fig.20, we show the volume covered by the 400d survey out to redshift z, for three representative X-ray luminosities, $L_x = 3\times10^{43}$, 10^{44}, and 3×10^{44} erg s^{-1}. Note that the volume for luminous clusters, $L_x \gtrsim 10^{44}$ erg s^{-1}at high redshifts exceeds the volume typically covered by the catalogs based on the *ROSAT* All-Sky Survey.

The effective volume as a function of *measured* X-ray luminosity, including first-order corrections for the Eddington bias (see § 7.2), is given by expressions

$$A_{\rm eff}(f_m,z) = A\,\frac{\iint P_m(f_m|f,r_c)\,P_d(f,r_c)\,n(f,r_c,z)\,dr_c\,df}{\int n(f_m,r_c,z)\,dr_c}, \qquad (9)$$

$$V_{\rm eff}(L_m,z_1,z_2) = \int_{z_1}^{z_2} A_{\rm eff}(f_m,z)\,\frac{dV}{dz}\,dz. \qquad (10)$$

This effective volume can be used for non-parametric estimation of the X-ray luminosity function from the 400d data, shown in Fig. 21 and 22 for the $z < 0.3$ and $z > 0.3$ subsamples, respectively. For comparison, we also show the low-z XLF from the REFLEX sample (Böhringer et al. 2002)[10] which is in very good agreement with our results, thus providing an independent proof that our flux measurements, calculations of the sky coverage etc., are accurate.

At $z > 0.3$ (Fig. 22), our XLF clearly shows negative evolution at high L_X compared with the low-redshift XLF. For example, the local XLF predicts that the 400d should contain 116 clusters with $L_x > 10^{44}$ erg s^{-1}at $z > 0.3$ while we found only 47 such objects ($\sim 7\sigma$ significance). The evolution is weaker for low-luminosity clusters; the total number of the $L_x < 10^{44}$ erg s^{-1}, $z > 0.3$ clusters in our sample is 17 while the non-evolving XLF predicts 29.5. Our XLF results are fully consistent with the earlier studies by Henry et al. (1992), Rosati et al. (1998), Vikhlinin et al. (1998b), Jones et al. (1998), Gioia et al. (2001), Mullis et al. (2004) but the evolution is measured with a much higher statistical significance because of the larger survey area.

To provide a quantitative characterization of the XLF evolution, we follow the approach of Rosati et al. (2002) and Mullis et al. (2004) to fit the data with the evolving Schechter (1976) model, $dN/dL = n\,L_*^{-1}\,(L/L_*)^{-\alpha}\,\exp(-L/L_*)$, where the normalization n and characteristic luminosity L_* are power-law functions of $(1+z)$,

$$n = n_0\,(1+z)^A \quad L_* = L_{*,0}(1+z)^B. \qquad (11)$$

The best-fit parameters obtained with the Maximum Likelihood approach Cash (1979) are $A = 0.05 \pm 0.82$ and $B = -1.43 \pm 0.39$.

8. *CHANDRA* OBSERVATIONS OF 400D CLUSTERS

A complete sample of high-redshift clusters from the 400d survey was observed by *Chandra* (PIs L. Van Speybroeck, S. S. Murray, A. Vikhlinin). Here, we use preliminary *Chandra* results to cross-check our X-ray flux estimates from the *ROSAT* data. Due to sufficiently long exposures, *Chandra* traced the cluster surface brightness to larger radii and thus provided accurate total fluxes without the need to rely on β-model fits. Figure 23 shows a comparison of *Chandra* fluxes with the *ROSAT* estimates. The horizontal line shows the flux limit of the 400d catalog. By design, all *ROSAT* fluxes are forced to be above this line, which leads to a significant bias at low f_x. Using the statistical calibrations described in § 6, we can predict this bias. Specifically, the average measured flux for clusters with true flux f is (cf. eq.2 and 3)

$$\langle f_m\rangle = \frac{\int_{f_{\rm min}}^{\infty} f_m\,df_m \int P_m(f_m|f,r_c)\,P_d(f,r_c)\,n(f,r_c)\,dr_c}{\int_{f_{\rm min}}^{\infty} df_m \int P_m(f_m|f,r_c)\,P_d(f,r_c)\,n(f,r_c)\,dr_c} \qquad (12)$$

where $f_{\rm min} = 1.4\times10^{-13}$ erg s^{-1} cm^{-2}. The predicted flux bias computed from eq.(12) is shown by the thick gray line in Fig.23. It agrees very well with the actually observed bias at $f \lesssim 2.5\times10^{-13}$ erg s^{-1} cm^{-2}. At higher fluxes, where one expects no selection biases, the *Chandra* and *ROSAT* fluxes agree to better than 10%: the average observed ratio is $f_{\rm ROSAT}/f_{\rm Chandra} = 1.02\pm0.04$. The comparison of our *ROSAT*-derived fluxes with the accurate *Chandra* measurements thus demonstrates the validity of the 400d statistical calibration and our cluster flux measurements procedure.

9. SUMMARY

We present a catalog of galaxy clusters detected in a new, 400 square degrees *ROSAT* PSPC survey. The survey uses the central 17.5′ region of 1610 individual pointings to high Galactic latitude targets, essentially all *ROSAT* PSPC data suitable for detection of high-redshift clusters. The X-ray analysis algorithm is adopted from that in the 160d survey Vikhlinin et al. (1998a) with minimal modifications. The 400d catalog includes 266 optically confirmed galaxy clusters, groups and individual elliptical galaxies with flux $f >$

[10] Other measurements based on the *ROSAT* All-Sky Survey, such as those from the BCS (Ebeling et al. 1997) or RASS1 Bright (de Grandi et al. 1999) catalogs, are consistent with the REFLEX result within the statistical uncertainties. We have chosen REFLEX because the XLF parameters are reported for the cosmology adopted here.

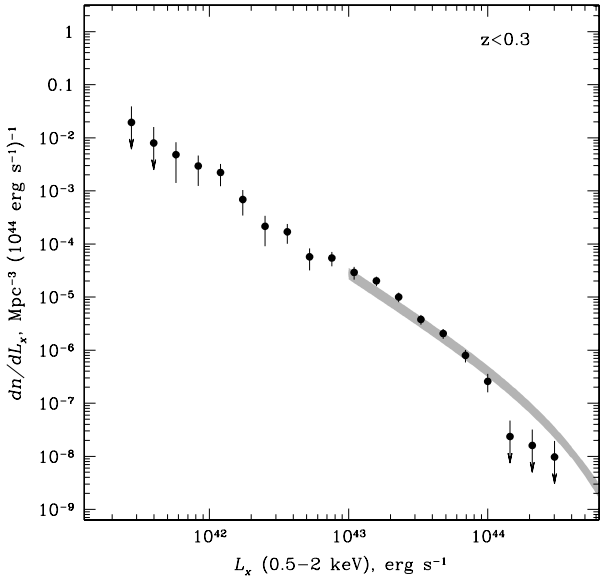

FIG. 21.— X-ray luminosity function for the 400d clusters at $z < 0.3$. The grey line shows the low-redshift XLF measured in the REFLEX survey. The width of the line corresponds to the uncertainties of the REFLEX XLF.

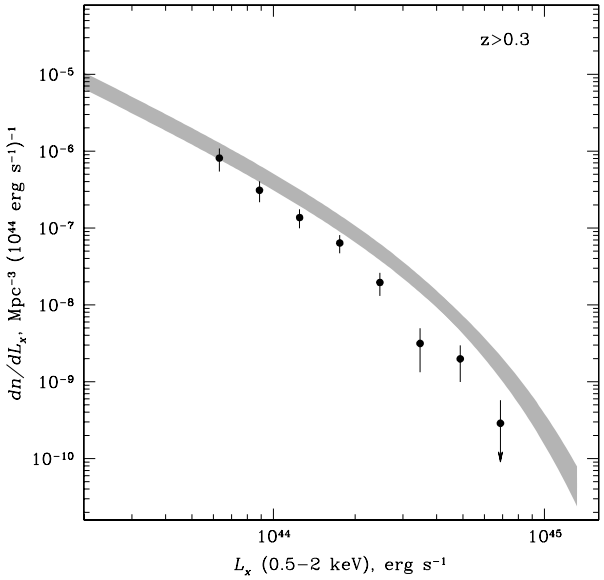

FIG. 22.— Same as Fig.21 but for the 400d clusters at $z > 0.3$.

1.4×10^{-13}erg s^{-1} cm^{-2} in 0.5–2 keV energy band. This sample is selected out of 287 candidate extended X-ray sources; the success rate of the X-ray selection is therefore very high, 93%. Redshifts of all clusters have been measured through optical spectroscopy (see Hornstrup et al., in preparation).

The statistical properties of the 400d sample have been carefully calibrated by extensive Monte-Carlo simulations. We provide the essential quantities, such as the cluster detection probability as a function of flux and size, and describe how to use them for calculations of the sky coverage or search volume in the given redshift interval. We also study the sensitivity of the statistical calibration to details of the cluster population models (e.g., the presence of the central X-ray brightness cusps caused by the radiative cooling). These analyses show that systematic uncertainties in the final area and volume calculations are within 5%, smaller than the Poisson uncertainties in our sample.

Our low-z X-ray luminosity function agrees very well with the results from the *ROSAT* All-Sky Survey. At $z \gtrsim 0.3$, the X-ray luminosity function shows negative evolution significant at $\sim 7\,\sigma$.

High-redshift clusters from the 400d catalog have been observed by *Chandra*. We will use these data to derive cosmological constraints (Vikhlinin et al., in preparation). Relevant to the present work is the comparison of the *ROSAT*-derived fluxes with the accurate values provided by the *Chandra* data. This comparison demonstrates the validity of the 400d statistical calibration and our cluster flux measurements procedure.

Machine-readable tables of our cluster catalog and associated calibration data are also published on the WWW pages `http://hea.iki.rssi.ru/400d` and `http://hea-www.harvard.edu/400d`.

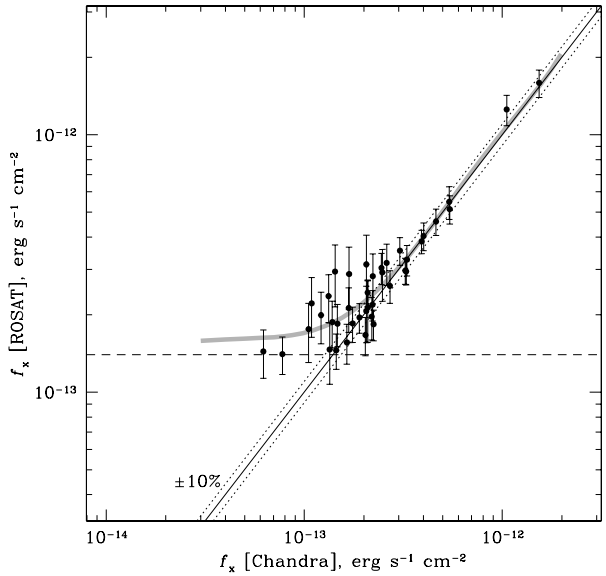

FIG. 23.— Comparison of the 400d cluster flux measurements with the accurate values derived from deep *Chandra* observations. The horizontal dashed lines indicates the flux limit of the 400d catalog. The thick gray line shows the expected average measured flux as a function of true flux (eq. 12).

We acknowledge the contribution of C. Mullis, B. R. McNamara, W. Forman, C. Jones, J. P. Henry, and I. Gioia to the "parent" project, the 160d *ROSAT* survey. We also thank P. Berlind, M. Calkins, M. Westover, J. E. Gonzalez, and G. Hertling for help with the optical observing and data reduction. We acknowledge generous support from the Time Allocation Committees of various optical telescopes including RTT-150 operated by the National Observatory of Turkey, Kazan State University, and IKI and Nordic Optical Telescope operated jointly by Denmark, Finland, Iceland, Norway, and Sweden, in the Spanish Observatorio del Roque de los Muchachos of the Instituto de Astrofisica de Canarias. Financial support was provided by NASA (grant NAG5-9217 and contract NAS8-39073), and grants from the Russian Academy of Sciences, Government, and Basic Research Foundation (02-02-16619, 05-02-16540, NSH-2083.2003.2, NSH-1100.2006.2, MK-4064.2005.2). HQ was partially supported by FONDAP Centro de Astrofisica.

REFERENCES

Abazajian, K., et al. 2005, AJ, 129, 1755
Abell, G. O., Corwin, Jr., H. G., & Olowin, R. P. 1989, ApJS, 70, 1
Appenzeller, I., et al. 1998, ApJS, 117, 319
Battye, R. A. & Weller, J. 2003, Phys. Rev. D, 68, 083506
Batuski, D. J., Miller, C. J., Slinglend, K. A., Balkowski, C., Maurogordato, S., Cayatte, V., Felenbok, P., & Olowin, R. 1999, ApJ, 520, 491
Bernardi, M., Alonso, M. V., da Costa, L. N., Willmer, C. N. A., Wegner, G., Pellegrini, P. S., Rité, C., & Maia, M. A. G. 2002, AJ, 123, 2990
Binggeli, B., Popescu, C. C., & Tammann, G. A. 1993, A&AS, 98, 275
Binggeli, B., Sandage, A., & Tammann, G. A. 1985, AJ, 90, 1681
Boese, F. G. 2000, A&AS, 141, 507
Böhringer, H., et al. 2000, ApJS, 129, 435
Böhringer, H., et al. 2002, ApJ, 566, 93
Bullock, J. S., Kolatt, T. S., Sigad, Y., Somerville, R. S., Kravtsov, A. V., Klypin, A. A., Primack, J. R., & Dekel, A. 2001, MNRAS, 321, 559
Burke, D. J., Collins, C. A., Sharples, R. M., Romer, A. K., & Nichol, R. C. 2003, MNRAS, 341, 1093
Cappi, A., Held, E. V., & Marano, B. 1998, A&AS, 129, 31
Cash, W. 1979, ApJ, 228, 939
Colless, M., et al. 2001, MNRAS, 328, 1039
Crawford, C. S. & Fabian, A. C. 2003, MNRAS, 339, 1163
da Costa, L. N., Pellegrini, P. S., Davis, M., Meiksin, A., Sargent, W. L. W., & Tonry, J. L. 1991, ApJS, 75, 935
da Costa, L. N., et al. 1998, AJ, 116, 1
de Grandi, S., et al. 1999, ApJ, 513, L17
de Vaucouleurs, G., de Vaucouleurs, A., Corwin, Jr., H. G., Buta, R. J., Paturel, G., & Fouque, P. 1991, S&T, 82, 621
Denicoló, G., Terlevich, R., Terlevich, E., Forbes, D. A., Terlevich, A., & Carrasco, L. 2005, MNRAS, 356, 1440
Ebeling, H., Edge, A. C., Fabian, A. C., Allen, S. W., Crawford, C. S., & Boehringer, H. 1997, ApJ, 479, L101
Ebeling, H., Edge, A. C., & Henry, J. P. 2001a, ApJ, 553, 668
Ebeling, H., Jones, L. R., Fairley, B. W., Perlman, E., Scharf, C., & Horner, D. 2001b, ApJ, 548, L23
Eddington, Sir, A. S. 1940, MNRAS, 100, 354
Eke, V. R., Cole, S., Frenk, C. S., & Patrick Henry, J. 1998, MNRAS, 298, 1145
Evrard, A. E. 1989, ApJ, 341, L71
Falco, E. E., et al. 1999, PASP, 111, 438
Fukazawa, Y., Makishima, K., Tamura, T., Ezawa, H., Xu, H., Ikebe, Y., Kikuchi, K., & Ohashi, T. 1998, 50, 187
Giacconi, R., et al. 1979, ApJ, 230, 540
Gioia, I. M., Henry, J. P., Maccacaro, T., Morris, S. L., Stocke, J. T., & Wolter, A. 1990a, ApJ, 356, L35
Gioia, I. M., Henry, J. P., Mullis, C. R., Böhringer, H., Briel, U. G., Voges, W., & Huchra, J. P. 2003, ApJS, 149, 29
Gioia, I. M., Henry, J. P., Mullis, C. R., Voges, W., Briel, U. G., Böhringer, H., & Huchra, J. P. 2001, ApJ, 553, L105
Gioia, I. M., Maccacaro, T., Schild, R. E., Wolter, A., Stocke, J. T., Morris, S. L., & Henry, J. P. 1990b, ApJS, 72, 567
Haiman, Z., Mohr, J. J., & Holder, G. P. 2001, ApJ, 553, 545
Hardcastle, M. J., Worrall, D. M., Birkinshaw, M., Laing, R. A., & Bridle, A. H. 2002, MNRAS, 334, 182
Hasinger, G., Burg, R., Giacconi, R., Hartner, G., Schmidt, M., Trumper, J., & Zamorani, G. 1993, A&A, 275, 1
Henry, J. P. 1997, ApJ, 489, L1
Henry, J. P. 2000, ApJ, 534, 565
Henry, J. P., Gioia, I. M., Maccacaro, T., Morris, S. L., Stocke, J. T., & Wolter, A. 1992, ApJ, 386, 408
Henry, J. P., Gioia, I. M., Mullis, C. R., Voges, W., Briel, U. G., Böhringer, H., & Huchra, J. P. 2001, ApJ, 553, L109
Hewitt, A. & Burbidge, G. 1991, ApJS, 75, 297
Hu, W. & Cohn, J. D. 2006, Phys. Rev. D, 73, 067301
Huchra, J. P., Geller, M. J., de Lapparent, V., & Corwin, Jr., H. G. 1990, ApJS, 72, 433
Huchra, J. P., Vogeley, M. S., & Geller, M. J. 1999, ApJS, 121, 287
Huterer, D. & Turner, M. S. 2001, Phys. Rev. D, 64, 123527
Jones, C. & Forman, W. 1999, ApJ, 511, 65
Jones, L. R., Ponman, T. J., Horton, A., Babul, A., Ebeling, H., & Burke, D. J. 2003, MNRAS, 343, 627
Jones, L. R., Scharf, C., Ebeling, H., Perlman, E., Wegner, G., Malkan, M., & Horner, D. 1998, ApJ, 495, 100
Katgert, P., Mazure, A., den Hartog, R., Adami, C., Biviano, A., & Perea, J. 1998, A&AS, 129, 399
Keel, W. C. 1996, ApJS, 106, 27
Kenter, A. T. & Murray, S. S. 2003, ApJ, 584, 1016
Kochanek, C. S., et al. 2001, ApJ, 560, 566
Lucey, J. R., Dickens, R. J., Mitchell, R. J., & Dawe, J. A. 1983, MNRAS, 203, 545
Mahdavi, A. & Geller, M. J. 2004, ApJ, 607, 202
Markevitch, M. 1998, ApJ, 504, 27
Mason, K. O., et al. 2000, MNRAS, 311, 456
Miller, C. J., Krughoff, K. S., Batuski, D. J., & Hill, J. M. 2002, AJ, 124, 1918
Miller, N. A., Owen, F. N., Hill, J. M., Keel, W. C., Ledlow, M. J., & Oegerle, W. R. 2004, ApJ, 613, 841
Mohr, J. J., Evrard, A. E., Fabricant, D. G., & Geller, M. J. 1995, ApJ, 447, 8
Molnar, S. M., Haiman, Z., Birkinshaw, M., & Mushotzky, R. F. 2004, ApJ, 601, 22
Molthagen, K., Wendker, H. J., & Briel, U. G. 1997, A&AS, 126, 509
Moretti, A., et al. 2004, A&A, 428, 21
Mullis, C. R., et al. 2003, ApJ, 594, 154
Mullis, C. R., et al. 2004, ApJ, 607, 175
Navarro, J. F., Frenk, C. S., & White, S. D. M. 1997, ApJ, 490, 493
Nesci, R. & Altamore, A. 1990, A&A, 234, 60
Oukbir, J. & Blanchard, A. 1992, A&A, 262, L21
Owen, F. N., Ledlow, M. J., & Keel, W. C. 1995, AJ, 109, 14
Perlman, E. S., Horner, D. J., Jones, L. R., Scharf, C. A., Ebeling, H., Wegner, G., & Malkan, M. 2002, ApJS, 140, 265
Peterson, B. M. 1978, ApJ, 223, 740
Ponman, T. J., Allan, D. J., Jones, L. R., Merrifield, M., McHardy, I. M., Lehto, H. J., & Luppino, G. A. 1994, Nature, 369, 462
Reiprich, T. H. & Böhringer, H. 2002, ApJ, 567, 716
Rines, K., Geller, M. J., Kurtz, M. J., & Diaferio, A. 2003, AJ, 126, 2152
Romer, A. K., et al. 2000, ApJS, 126, 209
Rosati, P., Borgani, S., & Norman, C. 2002, ARA&A, 40, 539
Rosati, P., della Ceca, R., Burg, R., Norman, C., & Giacconi, R. 1995, ApJ, 445, L11
Rosati, P., della Ceca, R., Norman, C., & Giacconi, R. 1998, ApJ, 492, L21
Scharf, C. A., Jones, L. R., Ebeling, H., Perlman, E., Malkan, M., & Wegner, G. 1997, ApJ, 477, 79
Schechter, P. 1976, ApJ, 203, 297
Schuecker, P., Böhringer, H., Collins, C. A., & Guzzo, L. 2003, A&A, 398, 867
Simien, F. & Prugniel, P. 2000, A&AS, 145, 263
Smith, R. J., Lucey, J. R., Hudson, M. J., Schlegel, D. J., & Davies, R. L. 2000, MNRAS, 313, 469
Snowden, S. L., McCammon, D., Burrows, D. N., & Mendenhall, J. A. 1994, ApJ, 424, 714
Starobinsky, A. A. 1998, JETP Lett., 68, 721
Stocke, J. T., Liebert, J., Schild, R., Gioia, I. M., & Maccacaro, T. 1984, ApJ, 277, 43
Stocke, J. T., Morris, S. L., Gioia, I. M., Maccacaro, T., Schild, R., Wolter, A., Fleming, T. A., & Henry, J. P. 1991, ApJS, 76, 813
Struble, M. F. & Rood, H. J. 1999, ApJS, 125, 35
Viana, P. T. P., Kay, S. T., Liddle, A. R., Muanwong, O., & Thomas, P. A. 2003, MNRAS, 346, 319
Viana, P. T. P. & Liddle, A. R. 1996, MNRAS, 281, 323
Viana, P. T. P. & Liddle, A. R. 1999, MNRAS, 303, 535
Vikhlinin, A. & Forman, W. 1995, ApJ, 455, L109
Vikhlinin, A., Forman, W., & Jones, C. 1999a, ApJ, 525, 47
Vikhlinin, A., McNamara, B. R., Forman, W., Jones, C., Quintana, H., & Hornstrup, A. 1998a, ApJ, 502, 558
Vikhlinin, A., McNamara, B. R., Forman, W., Jones, C., Quintana, H., & Hornstrup, A. 1998b, ApJ, 498, L21
Vikhlinin, A., McNamara, B. R., Hornstrup, A., Quintana, H., Forman, W., Jones, C., & Way, M. 1999b, ApJ, 520, L1
Vikhlinin, A., VanSpeybroeck, L., Markevitch, M., Forman, W. R., & Grego, L. 2002, ApJ, 578, L107
Vikhlinin, A., et al. 2003, ApJ, 590, 15
Voevodkin, A. & Vikhlinin, A. 2004, ApJ, 601, 610
Wang, L. & Steinhardt, P. J. 1998, ApJ, 508, 483
Wegner, G., Colless, M., Saglia, R. P., McMahan, R. K., Davies, R. L., Burstein, D., & Baggley, G. 1999, MNRAS, 305, 259
Wegner, G., et al. 2003, AJ, 126, 2268
White, S. D. M., Efstathiou, G., & Frenk, C. S. 1993, MNRAS, 262, 1023

APPENDIX

A. SUMMARY OF NOTATIONS

For quick reference, we provide a summary of notations used throughout the paper.

r_c — core-radius of the β-model; in calculations of the survey area and volumes, it is assumed to be in units of angular size;

f, f_x — true cluster flux in the 0.5–2 keV band;

f_m — measured flux in the 0.5–2 keV band;

$P_d(f, r_c)$ — the probability for the cluster to be detected and identified as extended X-ray source (§ 6.1);

$P_m(f_m|f, r_c)$ — the probability for the detected cluster to have measured flux f_m (§ 6.2);

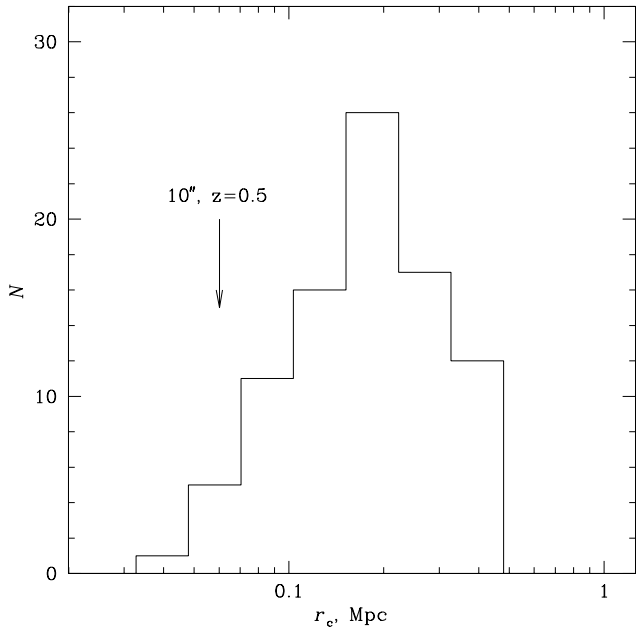

FIG. 24.— The distribution of cluster core radii in the Jones & Forman (1999) sample. The core radii have been corrected for the average trend with L_X. The arrow indicates the proper distance that corresponds to 10″ at $z = 0.5$ (approximately the angular size below which the discrimination of extended and point sources becomes ineffective).

$P_{\rm sel}$ — the probability that the cluster is detected and has f_m above the 400d catalog selection threshold (§ 7.1);
$n(f, r_c, z)$ — number density of clusters at redshift z as a function of true observed flux and angular size;
A — geometric area of the survey (intersection of the 18.5′ circles centered on individual pointings, minus the target regions);
$A_{\rm eff}(f_m)$ — effective sky coverage as a function of measured flux (§ 7.2);
$V(L)$ — comoving search volume for clusters with true luminosity L (§ 7.3);
$V_{\rm eff}(L_m)$ — effective comoving search volume as a function of measured luminosity L_m (§ 7.3);

B. REFERENCE MODEL OF THE CLUSTER POPULATION

The calculation of essential quantities such as the survey area or volume involves averaging of the detection probabilities over the expected distribution of cluster sizes and fluxes (§ 7). For this, we use the reference model which assumes a non-evolving population of β-model clusters with the distribution of structural parameters and the X-ray luminosity function fixed by detailed observations of the low-redshift objects, as detailed below.

The distribution of cluster core radii is taken from the *Einstein* sample of Jones & Forman (1999). The use of Jones & Forman sample is justified by the fact that nearby clusters at $z \approx 0.1$ were observed by *Einstein* approximately with the same proper-size resolution as *ROSAT* distant clusters at $z \approx 0.5$. The average core radius in the Jones & Forman sample shows a trend with the cluster luminosity which can be approximated as $r_c \propto L_x^{0.5}$ for $L_x < 10^{44}$ erg s^{-1} and constant average r_c at higher luminosities. We corrected individual r_c measurements in the Jones & Forman sample by this trend to obtain the master distribution of r_c shown in Fig. 24. The distribution for any luminosity is obtained by scaling the master distribution by the trend of average r_c with L_x. The distribution of β-parameters is also adopted from Jones & Forman (1999), with one modification. The Jones & Forman distribution contains objects with $\beta < 0.6$ and even $\beta < 0.5$. Such low values are unrealistic (e.g., the total flux diverges for $\beta \le 0.5$). They are artifacts of fitting a single β-model to the cluster with cool cores and are in fact not found if the cores are excluded from the fit (Vikhlinin et al. 1999a). For our work, the relevant slope is that at large radii (it affects the total flux estimates). Therefore, we truncated the Jones & Forman distribution at $\beta < 0.6$. Finally, our β-models are elliptical with the distribution of axis ratios from Mohr et al. (1995).

Our adopted X-ray luminosity function is the Schechter (1976) fit to the REFLEX survey data (Böhringer et al. 2002),

$$dN/dL = C\, L^{-\alpha}\, \exp(-L/L_*) \tag{B1}$$

with $\alpha = 1.69$ and $L_* = 2.57\times10^{44}$ erg s^{-1} (we use the Mullis et al. 2004, conversion of L_* to the 0.5–2 keV band). The REFLEX XLF is consistent with other *ROSAT* All-Sky Survey measurements (Ebeling et al. 1997; de Grandi et al. 1999). We use the REFLEX results because they are reported for our adopted cosmology.

To compute the survey area and search volume, we need the distribution of clusters as a function of observed flux, not the rest-frame luminosity (see § 7.1 and 7.3). This can be obtained from the luminosity function through an obvious relation,

$$dN/df = \text{const} \times dN/dL, \qquad f = \frac{L}{4\pi\, d_L(z)^2}\, K(z), \tag{B2}$$

where $d_L(z)$ is the cosmological luminosity distance and $K(z)$ is the K-correction factor that describes redshifting of the source spectrum. The K-correction can be easily computed for any given source spectrum (see, e.g., Jones et al. 1998, specifically for the

case of the cluster X-ray spectra). The K-correction in principle depends on the temperature and, more weakly, on the metallicity of the ICM. The temperature can be estimated from the $L_x - T$ correlation with the accuracy sufficient for this purpose. We use a non-evolving $L_x - T$ relation that follows the Markevitch (1998) measurements for the high-T clusters and the Fukazawa et al. (1998) data for low-mass clusters and groups. It is now established that the $L_x - T$ relation in fact evolves (Vikhlinin et al. 2002). However, this does not affect the luminosity-to-flux conversion because the evolution is not strong and the K-correction is a weak function of temperature in the high-T regime (see, e.g., Fig.7 in Jones et al. 1998).

TABLE 4
CLUSTER CATALOG

Num.	R.A. (J2000)	Dec. (J2000)	f_x, 10^{-13} cgs	z	z ref.	L_X, erg s^{-1}	Note
(1)	(2)	(3)	(4)	(5)	(6)	(7)	(8)
1	00:29:50.6	+13:30:14	3.14 ± 0.78	0.251		5.38×10^{43}	
2	00:30:33.6	+26:18:16	2.44 ± 0.29	0.500	1	1.85×10^{44}	VMF 001
3	00:45:18.8	−29:24:02	3.41 ± 0.49	0.257		6.12×10^{43}	
4	00:50:59.3	−09:29:14	3.66 ± 0.50	0.199	1	3.81×10^{43}	VMF 003
5	00:56:55.0	−22:13:51	2.48 ± 0.45	0.116	1	8.29×10^{42}	VMF 005
6	00:56:03.5	−37:32:43	14.92 ± 1.53	0.163	2	9.79×10^{43}	
7	00:57:24.7	−26:16:50	18.60 ± 2.23	0.113	3	5.66×10^{43}	VMF 007, A 0122
8	01:06:59.0	+32:09:30	4.53 ± 0.52	0.112	4	1.37×10^{43}	§ 4.1
9	01:13:11.0	+28:28:16	3.99 ± 0.97	0.262		7.41×10^{43}	
10	01:16:39.7	−03:30:11	3.22 ± 0.46	0.0810	5	5.02×10^{42}	
11	01:22:36.0	−28:32:05	2.69 ± 0.61	0.256	1	4.82×10^{43}	VMF 010, A S0154
12	01:24:48.1	+09:32:29	3.87 ± 0.46	0.0079	6	5.29×10^{40}	NGC 0524
13	01:26:54.5	+19:12:42	1.49 ± 0.43	0.0427	7	6.23×10^{41}	IC 0115, A 0195
14	01:32:54.6	−42:59:46	3.25 ± 0.81	0.0876	1	5.96×10^{42}	VMF 014
15	01:39:53.7	+18:10:07	2.73 ± 0.36	0.176	3	2.20×10^{43}	VMF 017, A 0227
16	01:41:32.3	−30:34:42	3.14 ± 0.94	0.442		1.81×10^{44}	§ 4.1
17	01:42:50.6	+20:25:13	2.61 ± 0.52	0.271	1	5.25×10^{43}	VMF 018
18	01:52:41.3	−13:58:13	1.84 ± 0.25	0.833	8	4.19×10^{44}	
19	01:54:12.5	−59:37:33	1.45 ± 0.36	0.360	1	5.55×10^{43}	VMF 020
20	01:59:18.2	+00:30:09	3.27 ± 0.45	0.386	1	1.40×10^{44}	VMF 021
21	02:06:49.9	−13:09:09	2.61 ± 0.49	0.321	1	7.59×10^{43}	VMF 023
22	02:09:52.8	−51:16:19	1.72 ± 0.66	0.206		1.95×10^{43}	
23	02:16:33.7	−17:47:27	1.40 ± 0.23	0.578	8	1.50×10^{44}	
24	02:23:28.2	−08:52:12	2.53 ± 0.34	0.163	9	1.73×10^{43}	
25	02:28:13.5	−10:05:45	2.43 ± 0.37	0.149	1	1.38×10^{43}	VMF 026
26	02:28:22.6	+23:25:23	2.59 ± 0.56	0.305		6.79×10^{43}	
27	02:30:26.6	+18:36:22	2.21 ± 0.58	0.799		4.59×10^{44}	
28	02:37:59.6	−52:24:47	7.33 ± 0.79	0.136	10	3.33×10^{43}	VMF 028, A 3038
29	02:45:45.7	+09:36:36	6.33 ± 2.05	0.147		3.41×10^{43}	
30	02:50:03.6	+19:07:51	2.59 ± 0.39	0.122	8	9.57×10^{42}	
31	02:51:17.8	−20:55:46	2.62 ± 0.55	0.325		7.84×10^{43}	
32	02:59:33.8	+00:13:45	3.24 ± 0.56	0.194	1	3.19×10^{43}	VMF 031
33	03:02:21.3	−04:23:29	15.89 ± 1.95	0.350		5.29×10^{44}	
34	03:04:24.7	−07:02:13	2.59 ± 0.67	0.135	11	1.19×10^{43}	
35	03:06:28.7	−09:43:50	10.40 ± 1.24	0.0342	12	2.71×10^{42}	IC 1880
36	03:07:04.7	−06:28:51	5.99 ± 0.82	0.347	11	2.01×10^{44}	
37	03:18:33.4	−03:02:56	4.60 ± 0.54	0.370	9	1.79×10^{44}	
38	03:20:18.1	−42:59:13	2.99 ± 0.67	0.158		1.92×10^{43}	
39	03:20:37.8	−43:11:52	2.62 ± 0.67	0.149		1.47×10^{43}	A S0343
40	03:22:59.4	−13:38:15	2.06 ± 0.68	0.334		6.62×10^{43}	
41	03:23:59.5	−19:16:34	3.26 ± 0.74	0.332		1.01×10^{44}	
42	03:27:54.5	+02:33:47	9.41 ± 1.00	0.0302	14	1.91×10^{42}	UGC 02748
43	03:28:36.1	−21:40:04	2.14 ± 0.57	0.590		2.33×10^{44}	
44	03:32:13.5	−29:10:39	4.83 ± 0.71	0.150	15	2.75×10^{43}	
45	03:33:10.2	−24:56:41	2.36 ± 0.50	0.475		1.61×10^{44}	
46	03:34:03.7	−39:00:49	6.43 ± 0.71	0.0623	3	3.86×10^{42}	A 3135
47	03:36:49.4	−28:04:53	9.46 ± 1.67	0.105	3	2.49×10^{43}	A 3141
48	03:38:11.8	−22:56:24	1.73 ± 0.23	0.173		1.35×10^{43}	
49	03:39:24.3	−33:13:09	3.46 ± 0.88	0.269		6.83×10^{43}	A 3150
50	03:40:51.6	−28:23:10	3.18 ± 0.58	0.346		1.08×10^{44}	
51	03:40:27.2	−28:40:20	17.77 ± 3.44	0.0680	3	1.90×10^{43}	A 3151
52	03:48:22.4	−33:28:33	10.38 ± 1.48	0.165	16	7.09×10^{43}	A 3169
53	03:50:43.9	−38:01:25	2.88 ± 0.78	0.363		1.09×10^{44}	§ 4.1
54	03:54:35.4	−37:45:20	19.72 ± 2.59	0.251		3.22×10^{44}	A 3184
55	03:54:34.6	−42:33:33	2.05 ± 0.55	0.224		2.77×10^{43}	
56	03:55:29.9	−36:34:03	10.84 ± 1.83	0.320	17	3.01×10^{44}	A S0400, MS 0353.6-3642
57	03:55:59.3	−37:41:46	2.92 ± 0.67	0.473		1.95×10^{44}	
58	04:05:24.3	−41:00:15	1.54 ± 0.37	0.686		2.35×10^{44}	

TABLE 4 — *Continued*

Num.	R.A. (J2000)	Dec.	f_X, 10^{-13} cgs	z	z ref.	L_X, erg s^{-1}	Note
(1)	(2)	(3)	(4)	(5)	(6)	(7)	(8)
59	04:17:25.8	−45:12:28	4.88 ± 1.05	0.213	15	5.81×10^{43}	A 3240
60	04:21:03.5	−46:29:34	3.51 ± 0.84	0.131		1.49×10^{43}	A 3247
61	04:22:28.8	−50:09:01	4.00 ± 1.18	0.0901		7.77×10^{42}	
62	04:28:42.4	−38:05:47	2.08 ± 0.55	0.154	3	1.27×10^{43}	VMF 036, A 3259
63	04:46:38.0	−04:21:02	7.71 ± 0.88	0.177		6.12×10^{43}	
64	04:58:55.1	−00:29:21	24.84 ± 2.61	0.0150	18	5.73×10^{41}	NGC 1713
65	05:05:58.2	−28:26:02	1.41 ± 0.21	0.131	1	6.12×10^{42}	VMF 038
66	05:06:04.0	−28:40:50	1.97 ± 0.41	0.136	1	9.18×10^{42}	VMF 039
67	05:09:43.4	−08:36:41	1.98 ± 0.26	0.125		7.72×10^{42}	
68	05:21:10.5	−25:30:36	1.76 ± 0.45	0.581	1	1.88×10^{44}	VMF 040
69	05:22:13.8	−36:24:49	1.84 ± 0.34	0.472	1	1.25×10^{44}	VMF 041
70	05:28:40.1	−32:51:29	1.99 ± 0.25	0.273	1	4.12×10^{43}	VMF 042
71	05:32:41.8	−46:14:17	4.11 ± 0.43	0.135	1	1.85×10^{43}	VMF 044
72	05:33:53.1	−57:46:45	1.70 ± 0.62	0.297	1	4.26×10^{43}	VMF 045
73	05:42:50.8	−41:00:05	2.19 ± 0.29	0.642		2.85×10^{44}	
74	05:44:13.3	−25:55:40	1.55 ± 0.33	0.260		2.91×10^{43}	foreground A 0548
75	06:10:32.0	−48:48:26	2.49 ± 0.28	0.243		3.99×10^{43}	
76	06:34:34.1	−62:26:46	2.77 ± 0.76	0.270		5.58×10^{43}	
77	06:35:28.4	−62:34:06	3.92 ± 0.84	0.157		2.46×10^{43}	a part of A 3398
78	07:20:53.7	+71:08:57	1.82 ± 0.24	0.230	19	2.62×10^{43}	
79	07:20:17.7	+71:32:11	1.48 ± 0.22	0.268	19	2.97×10^{43}	
80	08:09:41.0	+28:11:58	5.49 ± 0.80	0.399		2.49×10^{44}	§ 4.1
81	08:10:24.2	+42:16:19	23.89 ± 2.63	0.0640	1	2.24×10^{43}	VMF 047
82	08:19:54.7	+56:34:39	3.08 ± 0.52	0.260	1	5.68×10^{43}	VMF 050
83	08:20:26.6	+56:45:27	2.29 ± 0.48	0.0429	1	9.63×10^{41}	VMF 051
84	08:38:31.3	+19:48:17	5.25 ± 1.34	0.123		1.96×10^{43}	
85	08:41:07.4	+64:22:41	2.91 ± 0.32	0.343	1	9.73×10^{43}	VMF 056
86	08:49:11.4	+37:31:23	1.46 ± 0.27	0.240	1	2.32×10^{43}	VMF 062, a part of A 0708
87	08:52:32.9	+16:18:07	3.71 ± 0.68	0.0980	1	8.60×10^{42}	VMF 063
88	08:53:13.4	+57:59:44	1.99 ± 0.45	0.475	1	1.37×10^{44}	VMF 064
89	09:00:04.7	+39:20:24	3.48 ± 0.68	0.0951		7.57×10^{42}	
90	09:07:20.0	+16:39:25	14.87 ± 1.66	0.0756	20	1.98×10^{43}	VMF 068, A 0744
91	09:10:16.1	+60:12:17	1.42 ± 0.35	0.181		1.23×10^{43}	a part of A 0742
92	09:21:13.2	+45:28:44	2.39 ± 0.43	0.315	1	6.75×10^{43}	VMF 070
93	09:26:36.6	+12:42:59	1.67 ± 0.28	0.489	1	1.23×10^{44}	VMF 071
94	09:43:32.4	+16:40:02	2.31 ± 0.36	0.256	1	4.15×10^{43}	VMF 073
95	09:43:45.0	+16:44:13	2.12 ± 0.47	0.180	1	1.79×10^{43}	VMF 074
96	09:50:07.7	+70:33:58	3.20 ± 0.54	0.210		3.72×10^{43}	
97	09:53:44.6	+69:47:29	1.60 ± 0.20	0.214		1.98×10^{43}	
98	09:53:36.0	+70:54:29	9.07 ± 1.32	0.185		7.89×10^{43}	A 0875
99	09:56:02.8	+41:07:08	1.56 ± 0.28	0.587	1	1.71×10^{44}	VMF 079
100	09:58:19.3	+47:02:17	2.82 ± 0.62	0.390	21	1.25×10^{44}	
101	09:58:13.0	+55:16:06	4.82 ± 0.88	0.214	1	5.81×10^{43}	VMF 081, A 0899
102	10:02:07.7	+68:58:48	1.97 ± 0.37	0.500		1.51×10^{44}	§ 4.1
103	10:03:06.6	−19:25:47	2.77 ± 0.46	0.243		4.44×10^{43}	
104	10:03:04.5	+32:53:36	3.55 ± 0.44	0.416	22	1.79×10^{44}	
105	10:07:08.4	−20:31:26	1.43 ± 0.44	0.105		3.88×10^{42}	
106	10:10:15.8	+54:30:12	2.11 ± 0.30	0.0450	1	9.80×10^{41}	VMF 084
107	10:11:25.4	+54:50:06	2.00 ± 0.52	0.294	1	4.86×10^{43}	VMF 086
108	10:13:27.8	−01:36:42	2.28 ± 0.55	0.276		4.82×10^{43}	
109	10:13:36.9	+49:33:05	4.40 ± 1.05	0.133	1	1.95×10^{43}	VMF 087
110	10:18:00.9	+21:54:35	2.32 ± 0.42	0.240		3.65×10^{43}	
111	10:27:10.7	+39:08:06	4.63 ± 0.56	0.338		1.48×10^{44}	
112	10:33:51.9	+57:03:11	1.45 ± 0.37	0.0463	1	7.18×10^{41}	VMF 089
113	10:36:11.3	+57:13:31	1.88 ± 0.41	0.203	1	2.08×10^{43}	VMF 090
114	10:38:01.8	+41:46:38	2.71 ± 0.42	0.125	23	1.06×10^{43}	A 1056
115	10:39:31.3	+39:47:38	1.92 ± 0.46	0.0926		4.00×10^{42}	
116	10:42:24.3	−00:08:16	3.44 ± 0.47	0.139	24	1.67×10^{43}	
117	10:48:00.6	−11:24:11	1.85 ± 0.37	0.0650	1	1.84×10^{42}	VMF 091
118	10:58:12.6	+01:36:57	13.00 ± 1.82	0.0385	25	4.31×10^{42}	VMF 095, a part of A 1139
119	11:10:04.5	−29:57:06	1.71 ± 0.31	0.200		1.82×10^{43}	
120	11:16:54.7	+18:03:20	6.23 ± 0.79	0.0032	26	1.37×10^{40}	NGC 3607
121	11:17:30.1	+17:44:45	1.44 ± 0.31	0.547	1	1.36×10^{44}	VMF 098
122	11:20:58.3	+23:26:34	2.12 ± 0.42	0.562	1	2.08×10^{44}	VMF 100
123	11:20:07.6	+43:18:07	2.97 ± 0.34	0.600	9	3.30×10^{44}	
124	11:23:10.6	+14:09:40	1.82 ± 0.42	0.340	1	6.07×10^{43}	VMF 101
125	11:24:36.6	+41:55:55	4.02 ± 0.93	0.195	1	3.97×10^{43}	VMF 103

TABLE 4 — *Continued*

Num.	R.A. (J2000)	Dec.	f_X, 10^{-13} cgs	z	z ref.	L_X, erg s^{-1}	Note
(1)	(2)	(3)	(4)	(5)	(6)	(7)	(8)
126	11:27:45.4	+43:09:47	1.83 ± 0.53	0.181	17	1.58×10^{43}	MS 1125.3+4324
127	11:28:54.2	+42:52:00	1.69 ± 0.32	0.411		8.55×10^{43}	
128	11:35:54.4	+21:31:04	1.78 ± 0.38	0.133	1	7.93×10^{42}	VMF 104
129	11:38:43.2	+03:15:33	1.59 ± 0.34	0.127	1	6.46×10^{42}	VMF 105
130	11:42:06.3	+10:08:52	4.71 ± 0.65	0.119	3	1.63×10^{43}	A 1354
131	11:42:16.6	+10:27:02	3.26 ± 0.46	0.117		1.10×10^{43}	foreground A 135, § 4.1
132	11:42:04.5	+21:45:00	4.56 ± 1.29	0.131	1	1.95×10^{43}	VMF 106
133	11:46:26.9	+28:54:19	3.92 ± 0.52	0.149	1	2.19×10^{43}	VMF 107
134	11:52:35.7	+37:32:46	3.49 ± 0.62	0.230		4.95×10^{43}	
135	11:59:51.2	+55:31:56	7.42 ± 0.76	0.0808	11	1.14×10^{43}	VMF 110, MS 1157.3+5548
136	12:00:49.5	−03:27:30	1.85 ± 0.27	0.396	1	8.59×10^{43}	VMF 111
137	12:00:07.7	+68:09:07	3.67 ± 0.73	0.265	11	7.01×10^{43}	foreground A 1432
138	12:01:04.7	+12:09:31	4.77 ± 1.15	0.304		1.21×10^{44}	
139	12:02:13.7	+57:51:53	1.47 ± 0.39	0.677		2.19×10^{44}	
140	12:06:33.5	−07:44:24	12.88 ± 1.52	0.0680	1	1.38×10^{43}	VMF 114
141	12:11:16.0	+39:11:41	3.18 ± 0.37	0.340	17	1.04×10^{44}	VMF 115, MS 1208.7+3928
142	12:12:59.0	+27:27:13	7.93 ± 1.09	0.179		6.42×10^{43}	a part of A 1489
143	12:12:19.2	+27:33:14	12.54 ± 1.69	0.353		4.28×10^{44}	a part of A 1489
144	12:13:34.4	+02:53:57	1.43 ± 0.29	0.409	1	7.24×10^{43}	VMF 116
145	12:16:19.8	+26:33:21	1.54 ± 0.40	0.428	1	8.52×10^{43}	VMF 117
146	12:17:48.5	+22:55:16	3.00 ± 0.59	0.140		1.47×10^{43}	
147	12:17:43.7	+47:29:14	6.09 ± 0.64	0.270		1.19×10^{44}	
148	12:20:17.4	+75:22:12	9.53 ± 1.00	0.0059	14	7.07×10^{40}	NGC 4291
149	12:21:25.0	+49:18:07	2.07 ± 0.51	0.700	1	3.25×10^{44}	VMF 119
150	12:22:16.2	+25:59:40	1.89 ± 0.32	0.160		1.26×10^{43}	
151	12:22:01.9	+27:09:19	1.87 ± 0.39	0.472		1.27×10^{44}	
152	12:24:17.5	+75:31:39	1.44 ± 0.21	0.0056	14	9.77×10^{39}	NGC 4386
153	12:26:57.7	+33:32:50	2.94 ± 0.34	0.888	28	7.52×10^{44}	
154	12:26:22.2	+62:24:38	1.43 ± 0.43	0.398	11	6.79×10^{43}	
155	12:27:14.1	+08:58:15	4.14 ± 0.53	0.0873	29	7.54×10^{42}	
156	12:30:14.1	+23:26:04	3.13 ± 0.73	0.221		4.06×10^{43}	
157	12:31:45.6	+41:37:11	2.82 ± 0.34	0.176		2.26×10^{43}	
158	12:35:06.4	+41:17:44	3.01 ± 0.83	0.189		2.81×10^{43}	A 1565
159	12:36:28.6	+12:24:21	2.45 ± 0.38	0.0667	31	2.56×10^{42}	IC 3574
160	12:36:56.8	+25:50:27	2.52 ± 0.38	0.175		2.01×10^{43}	
161	12:48:36.4	−05:48:01	3.47 ± 0.47	0.0041	25	1.28×10^{40}	NGC 4697
162	12:52:04.7	−29:20:51	2.15 ± 0.40	0.188	1	2.00×10^{43}	VMF 124
163	12:53:04.7	+62:48:10	2.32 ± 0.45	0.235		3.45×10^{43}	A 1636
164	12:59:51.0	+31:20:48	5.68 ± 1.53	0.0523	5	3.56×10^{42}	
165	13:01:43.4	+10:59:35	2.80 ± 0.71	0.231	1	4.00×10^{43}	VMF 130
166	13:08:32.9	+53:42:15	1.69 ± 0.26	0.330	9	5.32×10^{43}	
167	13:11:12.7	+32:28:58	4.67 ± 0.56	0.245	1	7.49×10^{43}	VMF 132
168	13:12:19.4	+39:00:58	2.59 ± 0.38	0.404		1.24×10^{44}	
169	13:13:39.1	−32:50:41	2.55 ± 0.35	0.0518		1.58×10^{42}	
170	13:29:49.4	−33:10:23	1.80 ± 0.30	0.0511		1.09×10^{42}	
171	13:29:27.9	+11:43:23	12.73 ± 2.18	0.0228	4	1.12×10^{42}	VMF 136, NGC 5171, NGC 5176
172	13:31:31.0	+62:38:24	2.19 ± 0.42	0.219		2.82×10^{43}	
173	13:34:20.3	+50:31:05	1.85 ± 0.29	0.620	9	2.26×10^{44}	
174	13:38:05.7	−29:44:22	4.11 ± 0.49	0.189	17	3.81×10^{43}	MS 1335.2-2928
175	13:38:50.2	+38:51:18	5.98 ± 0.77	0.246	33	9.61×10^{43}	3C 28, § 4.1
176	13:40:54.0	+39:58:28	3.47 ± 0.66	0.169	1	2.55×10^{43}	VMF 145, A 1774
177	13:40:33.5	+40:17:46	1.61 ± 0.29	0.171	1	1.23×10^{43}	VMF 144
178	13:41:52.0	+26:22:49	80.95 ± 8.30	0.0755	3	1.06×10^{44}	VMF 146, A 1775
179	13:43:27.9	+55:46:55	1.99 ± 0.24	0.0673	11	2.13×10^{42}	VMF 150, a part of A 1783
180	13:49:00.2	+49:18:33	5.52 ± 0.96	0.167	22	3.88×10^{43}	a part of A 1804
181	13:54:16.7	−02:21:46	1.46 ± 0.23	0.546	1	1.37×10^{44}	VMF 151
182	13:57:19.4	+62:32:42	1.95 ± 0.26	0.525		1.67×10^{44}	
183	14:06:55.0	+28:34:16	2.56 ± 0.31	0.118	1	8.82×10^{42}	VMF 154
184	14:10:15.9	+59:38:27	2.01 ± 0.68	0.319	11	5.85×10^{43}	VMF 156
185	14:10:13.4	+59:42:38	3.35 ± 0.69	0.316	11	9.37×10^{43}	VMF 155
186	14:16:26.8	+23:15:31	13.05 ± 1.38	0.138	9	6.09×10^{43}	
187	14:16:28.1	+44:46:38	4.04 ± 0.50	0.400	1	1.86×10^{44}	VMF 158
188	14:18:31.2	+25:10:47	7.54 ± 0.78	0.290	1	1.71×10^{44}	VMF 159
189	14:27:58.2	+26:30:23	1.46 ± 0.23	0.0324	32	3.45×10^{41}	IC 4436
190	14:34:17.3	−32:29:04	12.63 ± 2.07	0.241		1.92×10^{44}	A S0766
191	14:36:58.4	+55:07:45	2.63 ± 0.54	0.125		1.03×10^{43}	
192	14:38:50.6	+64:23:39	2.62 ± 0.42	0.146	1	1.43×10^{43}	VMF 164

TABLE 4 — *Continued*

Num.	R.A. (J2000)	Dec.	f_X, 10^{-13} cgs	z	z ref.	L_X, erg s^{-1}	Note
(1)	(2)	(3)	(4)	(5)	(6)	(7)	(8)
193	14:48:36.2	−27:49:10	5.11 ± 1.08	0.175		3.99×10^{43}	may be a part of A 3609
194	14:51:17.4	+18:41:00	2.73 ± 0.56	0.0439	36	1.20×10^{42}	IC 1062
195	15:01:18.3	−08:30:33	14.00 ± 1.75	0.108		3.88×10^{43}	
196	15:04:39.1	−14:53:58	2.79 ± 0.76	0.284		6.24×10^{43}	
197	15:15:33.0	+43:46:35	3.45 ± 0.68	0.137	1	1.62×10^{43}	VMF 168
198	15:24:40.3	+09:57:35	3.04 ± 0.42	0.516	1	2.45×10^{44}	VMF 170
199	15:33:17.1	+31:08:55	18.17 ± 2.96	0.0673	3	1.90×10^{43}	A 2092
200	15:37:44.6	+12:00:21	2.67 ± 0.74	0.134	1	1.19×10^{43}	VMF 171
201	15:52:12.3	+20:13:42	4.97 ± 0.61	0.136	1	2.29×10^{43}	VMF 175
202	16:14:11.5	+34:25:25	2.30 ± 0.45	0.269		4.61×10^{43}	
203	16:29:46.1	+21:23:55	2.53 ± 0.53	0.184	1	2.24×10^{43}	VMF 178
204	16:30:14.7	+24:34:49	17.79 ± 2.54	0.0655	1	1.76×10^{43}	VMF 179
205	16:31:04.9	+21:21:54	3.01 ± 0.60	0.0980	1	6.99×10^{42}	VMF 180
206	16:39:55.5	+53:47:55	13.07 ± 1.43	0.111	1	3.84×10^{43}	VMF 182, A 2220
207	16:41:52.3	+40:01:29	2.94 ± 0.80	0.464	1	1.88×10^{44}	VMF 184
208	16:41:11.0	+82:32:26	8.03 ± 1.16	0.206	1	8.79×10^{43}	VMF 183
209	16:58:33.9	+34:30:08	3.37 ± 0.68	0.330	1	1.03×10^{44}	VMF 187
210	17:00:42.7	+64:12:58	4.56 ± 0.48	0.225	3	6.10×10^{43}	VMF 189, A 2246
211	17:01:22.6	+64:14:09	3.85 ± 0.40	0.453	1	2.32×10^{44}	VMF 190
212	17:22:53.9	+41:05:30	2.87 ± 0.63	0.309	1	7.69×10^{43}	VMF 193
213	17:29:00.6	+74:40:40	1.74 ± 0.51	0.213	1	2.13×10^{43}	VMF 194
214	17:46:27.4	+68:48:57	2.23 ± 0.34	0.217	1	2.81×10^{43}	VMF 195
215	17:51:08.6	+65:31:59	3.41 ± 0.71	0.0428	32	1.42×10^{42}	NGC 6505
216	17:51:38.6	+67:19:19	4.81 ± 1.42	0.0933	40	1.00×10^{43}	
217	18:06:55.8	+65:37:11	4.93 ± 1.00	0.263	40	9.15×10^{43}	
218	18:07:28.1	+69:46:22	1.41 ± 0.39	0.0941		3.04×10^{42}	
219	18:19:10.0	+69:09:39	2.58 ± 0.89	0.205		2.88×10^{43}	
220	18:23:43.5	+56:58:26	2.59 ± 0.41	0.105		7.03×10^{42}	
221	18:46:42.7	−74:31:59	4.53 ± 0.75	0.141		2.25×10^{43}	
222	20:03:13.3	−32:47:31	2.53 ± 0.61	0.256		4.54×10^{43}	
223	20:03:28.4	−55:56:47	4.77 ± 0.60	0.0148	41	2.29×10^{41}	VMF 196, A S0840
224	20:11:53.2	−35:55:40	2.13 ± 0.52	0.172		1.65×10^{43}	
225	20:51:38.6	−57:04:24	1.43 ± 0.24	0.0599		1.20×10^{42}	
226	21:14:19.8	−68:00:56	2.57 ± 0.30	0.130	1	1.09×10^{43}	VMF 201
227	21:37:51.2	−42:51:08	5.08 ± 0.66	0.185		4.46×10^{43}	A 3791
228	21:37:06.9	+00:26:48	2.77 ± 0.63	0.0509	1	1.65×10^{42}	VMF 202
229	22:13:30.4	−16:56:05	1.83 ± 0.36	0.297	1	4.57×10^{43}	VMF 207
230	22:20:09.1	−52:28:01	18.80 ± 2.22	0.102	42	4.64×10^{43}	A 3864
231	22:22:13.9	−52:35:13	2.61 ± 0.41	0.174		2.05×10^{43}	may be a part of A 3870
232	22:39:38.8	−05:43:13	3.24 ± 0.46	0.243	8	5.15×10^{43}	VMF 210, a part of A 2465
233	22:39:24.4	−05:46:57	2.22 ± 0.32	0.242	8	3.54×10^{43}	VMF 208, a part of A 2465
234	22:47:29.5	+03:37:08	2.30 ± 0.50	0.200	1	2.44×10^{43}	VMF 211
235	22:58:07.1	+20:55:06	5.06 ± 0.60	0.288	17	1.14×10^{44}	VMF 213, MS 2255.7+2039
236	23:05:25.7	−35:45:43	1.55 ± 0.29	0.201	1	1.67×10^{43}	VMF 214
237	23:18:05.5	−42:35:34	1.56 ± 0.30	0.209	1	1.83×10^{43}	VMF 216
238	23:19:34.2	+12:26:12	3.83 ± 0.49	0.126	1	1.49×10^{43}	VMF 217
239	23:23:14.8	+18:11:23	5.04 ± 0.99	0.154		3.02×10^{43}	
240	23:25:39.0	−54:43:57	2.26 ± 0.68	0.102	1	5.78×10^{42}	VMF 218
241	23:48:53.4	−31:17:12	3.25 ± 0.44	0.184	1	2.85×10^{43}	VMF 221, A 4043
242	23:55:11.5	−15:00:29	2.66 ± 0.65	0.0857	1	4.69×10^{42}	VMF 223

NOTE. — Cluster redshift references are: 1 — Vikhlinin et al. (1998a); Mullis et al. (2003); 2 — Cappi et al. (1998); 3 — Struble & Rood (1999); 4 — Mahdavi & Geller (2004); 5 — Rines et al. (2003); 6 — Simien & Prugniel (2000); 7 — Huchra et al. (1999); 8 — Perlman et al. (2002); 9 — Romer et al. (2000); 10 — Nesci & Altamore (1990); 11 — Abazajian et al. (2005); 12 — da Costa et al. (1998); 13 — Abell et al. (1989); 14 — de Vaucouleurs et al. (1991); 15 — Colless et al. (2001); 16 — Batuski et al. (1999); 17 — Stocke et al. (1991); 18 — Wegner et al. (2003); 19 — Mason et al. (2000); 20 — Peterson (1978); 21 — Molthagen et al. (1997); 22 — Böhringer et al. (2000); 23 — Miller et al. (2002); 24 — Appenzeller et al. (1998); 25 — Smith et al. (2000); 26 — Denicoló et al. (2005); 27 — Binggeli et al. (1985); 28 — Ebeling et al. (2001b); 29 — Burke et al. (2003); 30 — Bernardi et al. (2002); 31 — Binggeli et al. (1993); 32 — Falco et al. (1999); 33 — Hewitt & Burbidge (1991); 34 — Keel (1996); 35 — Huchra et al. (1990); 36 — Wegner et al. (1999); 37 — Miller et al. (2004); 38 — Owen et al. (1995); 39 — Kochanek et al. (2001); 40 — Gioia et al. (2003); 41 — da Costa et al. (1991); 42 — Katgert et al. (1998); If redshift reference is missing, the redshift is our measurement The codes in column (8) are VMF — 160d cluster (Vikhlinin et al. 1998a; Mullis et al. 2003); A — Abell cluster (Abell et al. 1989); MS — EMSS (Stocke et al. 1991).

TABLE 5
CLUSTERS AT *ROSAT* TARGET z

Num.	R.A. (J2000)	Dec.	f_X, 10^{-13} cgs	z	z ref.	L_X, erg s^{-1}	Note	*ROSAT* target: z	Type	Name
(1)	(2)	(3)	(4)	(5)	(6)	(7)	(8)	(9)	(10)	(11)
1	03:22:20.5	−49:18:42	4.04 ± 0.66	0.0670	13	4.23×10^{42}	VMF 032, A S0346	0.0710	AGN	2MASX J03231532−4931064
2	03:31:59.4	−45:24:24	1.63 ± 0.36	0.0671		1.73×10^{42}		0.0665		Horologium Supercluster (Lucey et al. 1983)
3	08:38:10.4	+25:06:02	18.48 ± 3.02	0.0286	4	3.34×10^{42}	CGCG 120-014	0.0286	AGN	NGC 2622, MKN 1218
4	10:20:45.3	+38:31:28	5.16 ± 0.65	0.0530		3.32×10^{42}		0.0491	GClstr	RX J1022.1+3830
5	10:24:19.1	+68:04:56	5.46 ± 0.62	0.201	9	5.72×10^{43}	A 0981	0.2031	GClstr	A 0998
6	12:04:04.0	+28:07:08	10.25 ± 1.09	0.167	17	7.17×10^{43}	VMF 112, MS 1201.5+2824	0.1653	AGN	GQ Com
7	12:36:59.5	+63:11:18	19.75 ± 2.22	0.302	3	4.78×10^{44}	A 1576	0.2970	BL Lac	HB89 1235+632
8	13:29:39.3	+29:46:05	2.25 ± 0.34	0.0473	32	1.16×10^{42}	CGCG 161-067	0.0470	AGN	VCV2001 J132908.8+295023
9	13:59:34.0	+62:19:01	4.93 ± 0.54	0.332		1.51×10^{44}		0.3280	GClstr	ZwCl 1358.1+6245
10	14:25:04.5	+37:58:16	2.04 ± 0.41	0.163		1.39×10^{43}		0.1712	GClstr	A 1914
11	14:44:06.4	+63:44:54	1.74 ± 0.38	0.298	35	4.38×10^{43}	VMF 165, A 1969	0.2990	BL Lac	MS 1443.5+6349
12	15:00:02.6	+22:34:05	1.46 ± 0.42	0.230	1	2.12×10^{43}	VMF 166	0.2350	BL Lac	FBQS J150101.8+223806
13	15:14:22.0	+36:36:22	5.14 ± 0.65	0.372	17	2.01×10^{44}	MS 1512.4+3647	0.3707	QSO	HB89 1512+370
14	15:36:35.3	+01:33:20	7.14 ± 1.83	0.309		1.87×10^{44}		0.3120	BL Lac	RBS 1517
15	15:40:10.1	+66:11:18	3.29 ± 0.59	0.245	37	5.34×10^{43}		0.2465	GClstr	A 2125
16	15:41:10.7	+66:26:30	2.91 ± 0.39	0.245	9	4.72×10^{43}		0.2465	GClstr	A 2125
17	15:47:20.4	+20:57:01	2.54 ± 0.88	0.266	1	4.93×10^{43}	VMF 174	0.2643	QSO	PG 1545+210
18	16:20:21.6	+17:23:19	2.08 ± 0.39	0.112	1	6.44×10^{42}	VMF 177	0.1124	QSO	MRK 0877, PG1617+175
19	16:27:00.1	+55:28:18	21.06 ± 2.44	0.130	3	8.61×10^{43}	A 2201	0.1330	QSO	SBS 1626+554
20	16:59:02.1	+32:29:15	3.37 ± 0.48	0.0621	38	3.03×10^{42}		0.0635	GClstr	A 2241
21	17:01:27.9	+34:00:35	3.72 ± 0.74	0.0960	11	8.25×10^{42}		0.0968	GClstr	A 2244
22	17:22:15.4	+30:42:45	12.22 ± 2.04	0.0467	39	6.02×10^{42}	CGCG 170-018	0.0430	AGN	MRK506
23	18:43:30.6	+79:49:57	3.15 ± 0.42	0.0510	17	1.88×10^{42}	MS 1846.9+7947	0.0561	AGN	3C 390.3
24	21:39:04.8	−23:33:08	5.18 ± 0.69	0.320		1.47×10^{44}		0.3130	GClstr	MS 2137.3−2353

NOTE. — See notes to Table 4

TABLE 6
OTHER EXTENDED X-RAY SOURCES

R.A. (J2000) (1)	Dec. (2)	f_X, 10^{-13} cgs (3)	z (4)	z ref. (5)	L_X, erg s^{-1} (6)	Type (7)	Note (8)
09:55:18.0	+69:50:57	2.48 ± 0.32	···		···	M82 wind	
12:19:09.9	+47:05:40	1.41 ± 0.18	0.0009	14	2.49×10^{38}	dE	UGC 07356
12:21:56.1	+04:29:09	4.38 ± 0.71	0.0052	27	2.58×10^{40}	SAB, Sy2	MESSIER 061
12:30:01.0	+13:38:41	4.62 ± 0.71	0.0045	30	2.04×10^{40}	SB0, Sy2	NGC 4477
14:13:15.1	−03:12:36	26.05 ± 2.80	0.0062	34	2.15×10^{41}	Sa, Sy2	NGC 5506

NOTE. — See notes to Table 4

TABLE 7
FALSE DETECTIONS

R.A. (J2000) (1)	Dec. (2)	f_X, 10^{-13} cgs (3)	Note (4)
03:22:26.4	−21:08:34	9.15 ± 1.49	
03:55:46.9	−39:25:23	2.30 ± 0.41	
05:22:37.1	−36:28:53	1.41 ± 0.41	
06:54:15.9	+69:05:52	1.44 ± 0.46	
10:07:09.9	+35:02:47	1.54 ± 0.24	
11:39:58.6	+31:53:04	1.45 ± 0.36	
12:30:35.6	+76:59:34	1.55 ± 0.49	
12:43:50.8	+02:44:12	3.22 ± 0.76	
13:37:54.2	+38:54:01	1.43 ± 0.41	VMF 143
14:18:45.6	+06:44:02	1.64 ± 0.24	VMF 160
14:28:28.0	+01:06:31	1.41 ± 0.29	
15:00:51.3	+22:44:56	1.78 ± 0.35	VMF 16, § 4.1
17:58:26.0	+65:30:58	3.93 ± 0.53	
19:58:02.6	−57:35:39	1.98 ± 0.65	
20:05:13.5	−56:12:57	3.51 ± 0.49	VMF 198
22:01:54.9	−51:24:04	1.53 ± 0.37	